

The Atacama Cosmology Telescope: Two-season ACTPol Extragalactic Point Sources and their Polarization properties

Rahul Datta,^{1★} Simone Aiola,² Steve K. Choi,² Mark Devlin,³ Joanna Dunkley,² Rolando Dünner,⁴ Patricio A. Gallardo,⁵ Megan Gralla,⁶ Mark Halpern,⁷ Matthew Hasselfield,^{8,9} Matt Hilton,¹⁰ Adam D. Hincks,¹¹ Shuay-Pwu P. Ho,² Johannes Hubmayr,¹² Kevin M. Huffenberger,¹³ John P. Hughes,¹⁴ Arthur Kosowsky,¹⁵ Carlos H. López-Caraballo,⁴ Thibaut Louis,¹⁶ Marius Lungu,² Tobias Marriage,¹⁷ Loïc Maurin,⁴ Jeff McMahon,¹⁸ Kavilan Moodley,¹⁰ Sigurd K. Naess,¹⁹ Federico Nati,³ Michael D. Niemack,⁵ Lyman A. Page,² Bruce Partridge,²⁰ Heather Prince,² Suzanne T. Staggs,² Eric R. Switzer,¹ and Edward J. Wollack¹

¹NASA/Goddard Space Flight Center, Greenbelt, MD 20771

²Joseph Henry Laboratories of Physics, Jadwin Hall, Princeton University, Princeton, NJ 08544

³Department of Physics and Astronomy, University of Pennsylvania, 209 South 33rd Street, Philadelphia, PA 19104

⁴Instituto de Astrofísica and Centro de Astro-Ingeniería, Pontificia Universidad Católica de Chile, Av. Vicuña Mackenna 4860, Santiago, Chile

⁵Department of Physics, Cornell University, Ithaca, NY 14853, USA

⁶Steward Observatory, University of Arizona, 933 N Cherry Avenue, Tucson, AZ 85721, USA

⁷Department of Physics and Astronomy, University of British Columbia, Vancouver, BC, Canada V6T 1Z4

⁸Department of Astronomy and Astrophysics, The Pennsylvania State University, University Park, PA 16802

⁹Institute for Gravitation and the Cosmos, The Pennsylvania State University, University Park, PA 16802

¹⁰Astrophysics and Cosmology Research Unit, University of KwaZulu-Natal, Westville Campus, Durban 4041, South Africa

¹¹Department of Physics, University of Rome "La Sapienza", Piazzale Aldo Moro 5, I-00185 Rome, Italy

¹²NIST Quantum Devices Group, 325 Broadway, Mailcode 817.03, Boulder, CO 80305, USA

¹³Department of Physics, Florida State University, Tallahassee FL 32306

¹⁴Department of Physics and Astronomy, Rutgers, The State University of New Jersey, Piscataway, NJ 08854-8019

¹⁵Department of Physics and Astronomy, University of Pittsburgh, Pittsburgh PA 15260 USA

¹⁶Laboratoire de l'Accélérateur Linéaire, Univ. Paris-Sud, CNRS/IN2P3, Université Paris-Saclay, Orsay, France

¹⁷Department of Physics and Astronomy, The Johns Hopkins University, 3400 N. Charles St., Baltimore, MD 21218-2686

¹⁸Department of Physics, University of Michigan, Ann Arbor, USA 48109

¹⁹Center for Computational Astrophysics, 162 5th Ave, New York, NY 10003

²⁰Department of Physics and Astronomy, Haverford College, Haverford, PA, USA 19041

10 March 2022

ABSTRACT

We report on measurements of the polarization of extragalactic sources at 148 GHz made during the first two seasons of the Atacama Cosmology Telescope Polarization (ACTPol) survey. The survey covered 680 deg² of the sky on the celestial equator. Polarization measurements of 169 intensity-selected sources brighter than 30 mJy, that are predominantly Active Galactic Nuclei, are presented. Above a total flux of 215 mJy where the noise bias removal in the polarization measurement is reliable, we detect 26 sources, 14 of which have a detection of linear polarization at greater than $3\sigma_p$ significance. The distribution of the fractional polarization as a function of total source intensity is analyzed. Our result is consistent with the scenario that the fractional polarization of our measured radio source population is independent of total intensity down to the limits of our measurements and well described by a Gaussian distribution with a mean fractional polarization $p = 0.028 \pm 0.005$ and standard deviation $\sigma_p = 0.054$, truncated at $p = 0$. Extrapolating this model for the distribution of source polarization below the ACTPol detection threshold, we predict that one could get a clean measure of the E-mode polarization power spectrum of the microwave background out to $\ell = 6000$ with $1 \mu\text{K}$ -arcminute maps over 10% of the sky from a future survey. We also study the spectral energy distribution of the total and polarized source flux densities by cross-matching with low radio frequency catalogs. We do not find any correlation between the spectral indices for total flux and polarized flux.

Key words: catalogues – surveys – active galactic nuclei – polarization – observational cosmology – cosmic microwave background

1 INTRODUCTION

The increasing sensitivity of millimeter wavelength telescopes has enabled detections of a large number of extragalactic sources that emit brightly in the millimeter-wavelength sky. These sources can be broadly categorized into two populations: active galactic nuclei (AGN), which are compact regions at the centre of galaxies, and dust-obscured star forming galaxies (DSFG), which represent the most intense starbursts in the universe. The radio emission from galaxies is typically dominated by synchrotron and free-free radiation.

In AGN, relativistic jets powered by the central nuclei accelerate electrons to relativistic velocities. These electrons then emit synchrotron radiation as they interact with the galactic magnetic field. In these so-called blazars (Angel & Stockman 1980), that are members of a larger group of active galaxies that host AGN, synchrotron self-absorption is associated with doppler-boosted structures along the jets and extends from radio to millimeter wavelengths. Free-free emission, also known as thermal bremsstrahlung, is emitted by free electrons interacting with ions in the ionized gas. The characterization of the blazar emission at millimeter (mm) and submillimeter (sub-mm) wavelengths is important for understanding the physics of these sources (Planck Collaboration et al. 2011).

The DSFGs are characterized by thermal radiation spanning millimeter to far infrared wavelengths emitted by dust heated by the UV and optical emission from massive stars in star-forming galaxies. This dust obscuration hides the DSFGs from optical and UV observatories. Observations at mm and sub-mm wavelengths can provide a more complete picture of the history of star formation (Casey et al. 2014). At these wavelengths, the brightest high redshift DSFGs are detected predominantly through their gravitational lensing (Vieira et al. 2013). In the mm/sub-mm regime, the radio emission is characterized by falling spectra with frequency, while the spectra of the dust emission increases steeply with frequency. Consequently, bright sources in the sky at wavelengths longer than 1.5 mm are predominantly radio sources, whereas dusty galaxies dominate the submillimeter sky, especially at low flux density. The Second Planck Catalog of Compact Sources (Planck Collaboration et al. 2016) spanning nine frequency channels captured this transition from radio sources to dusty galaxies. They found that the change in the dominant source population occurs between 217 and 353 GHz in frequency, i.e., 1.382 and 0.850 mm in wavelength.

The emission from both types of sources contaminates measurements of the CMB, which contains information on cosmological parameters. The measurement of the CMB polarization, particularly the E-mode damping tail, can help break some of the degeneracies between cosmological parameters. Measurements of the polarization damping tail are expected to become foreground-limited at a smaller angular scale (higher ℓ) than the temperature damping tail, because of the expected low polarization of dusty point sources (see below). Further, the higher contrast of the acoustic features in EE power spectrum compared to astrophysical foregrounds (Galli et al. 2014; Calabrese et al. 2014) will ultimately provide independent and tighter constraints on the standard cosmological parameters, such as the scalar spec-

tral index n_s , than those from the temperature data alone. High-resolution measurements of the E-mode polarization will improve the delensing of the primordial B-modes (Seljak & Hirata 2004), ultimately tightening the constraint on the tensor-to-scalar ratio r . As measurements of the small angular-scale fluctuations in the CMB are attaining higher sensitivity and finer resolution, ongoing and planned ground-based CMB surveys, such as Advanced ACTPol (Henderson et al. 2016), SPT-3G (Benson et al. 2014), Simons Observatory (SO 2017), CCAT-prime (CCAT-prime 2017), and CMB Stage 4 (Abazajian et al. 2016; Abitbol et al. 2017) will be capable of extracting information from the E-mode damping tail out to $\ell \approx 9000$. However, the contribution of the extragalactic point sources to the CMB power spectrum increases towards smaller angular scales, and it is expected to be a significant fraction of the CMB polarization power. For example, extragalactic foreground sources are expected to be the predominant contaminant for angular scales smaller than $30'$ ($\ell \gtrsim 400$) in the 70–100 GHz frequency range (Tofolatti et al. 1998). Hence, characterization of these sources in terms of their spectral and spatial distributions is essential for separating foregrounds from the CMB.

Measurement of the polarization properties of extragalactic radio sources, in itself, opens up an interesting way to study the astrophysics of the sources. Sources detected in polarization up to about 200 GHz are expected to be mostly radio sources, while the number of detected dusty galaxies increases with increasing frequency. For radio-loud AGNs, polarization data at mm/sub-mm wavelengths reveals details of the magnetic fields in the unresolved regions of their relativistic jets (Nartallo et al. 1998). The degree of linear polarization of synchrotron emission could be intrinsically as high as 60–80% (Saikia & Salter 1988). However, observed polarization fractions for compact extragalactic radio sources are typically well below 10%, which is believed to be the result of vector averaging along the line of sight. Nonetheless, at least some sources can have higher polarization fractions, up to 20% for individual sources (Huffenberg et al. 2015).

Also, little is known about the degree of polarization of DSFGs, but it is likely to be low because the complex structure of galactic magnetic fields with reversals along the line of sight and the disordered alignment of dust grains reduce the global polarized flux when integrated over the whole galaxy. Greaves & Holland (2002) and Matthews et al. (2009) have reported polarization measurements at 850 μm for two galaxies, M82 and M87, respectively. They found M82 to have a global net polarization of only 0.4%. Seiffert et al. (2007) placed an upper limit of 1.54% on the polarized emission from the ultra luminous infrared galaxy (ULIRG) Arp 220 at 850 μm . Trombetti et al. (2018) analyzed the fractional polarization of extragalactic sources in Planck maps and placed 90% confidence upper limits of 2.2% at 353 GHz and 3.9% at 217 GHz on the polarization fraction of dusty sources.

Compared to arcsecond resolution radio telescopes with very high sensitivity, millimeter wavelength telescopes have only recently achieved the required sensitivity at arcminute level resolution to detect large numbers of compact extragalactic sources. Thousands of such sources are being detected in CMB maps as high, point-like (unresolved) fluctuations above the background fluctuation level. While the

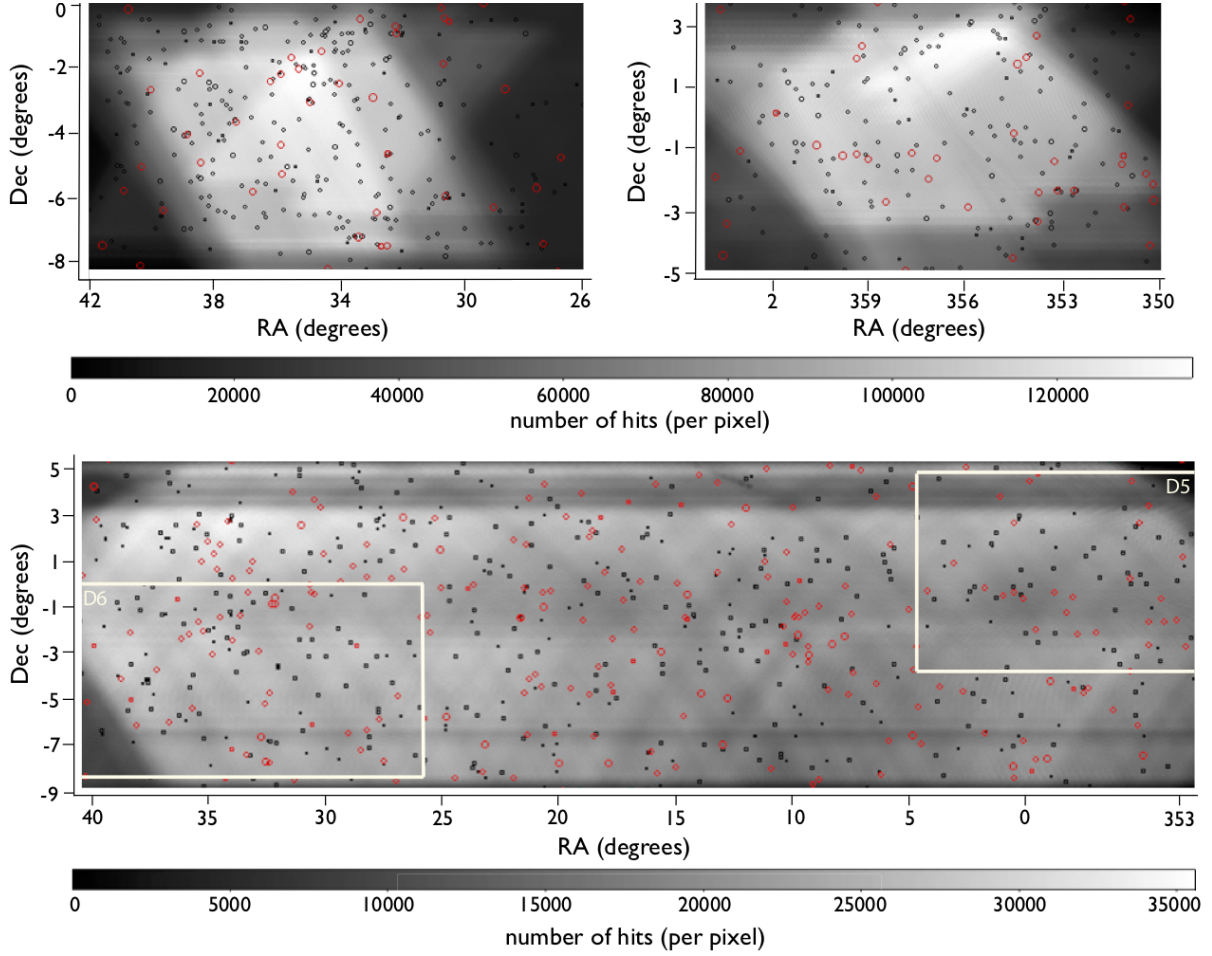


Figure 1. Sources detected in the S13+S14 D6 (left top), D5 (right top) and S14 D56 (bottom) maps shown with the hit count maps in the background. The red circles are $1'$ in diameter and centered at the locations of detected sources brighter than 20 mJy. The black circles are $0.5'$ in diameter and centered at the locations of sources detected with $S/N > 4.5$ that are dimmer than 20 mJy. D5 and D6 are contained within the boundaries of D56 but were observed at a different time (Louis et al. 2017).

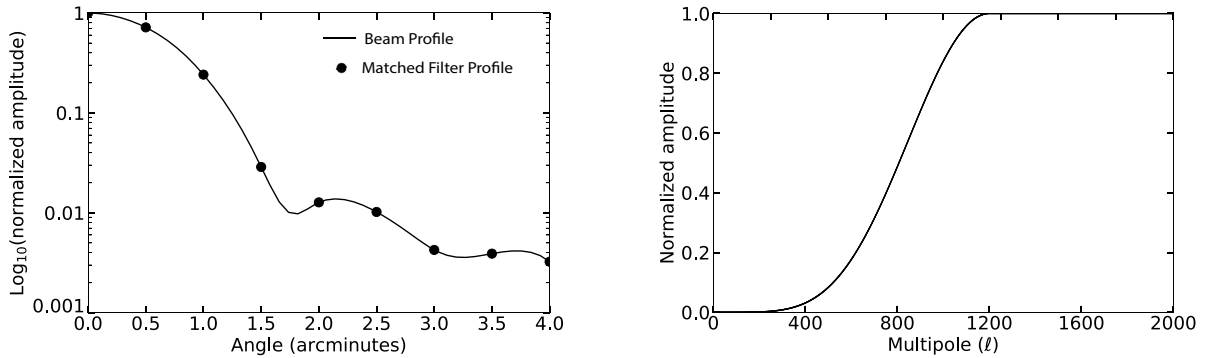


Figure 2. *Left:* The solid curve shows the unit normalized best-fit ACTPol beam profile. The beam FWHM (full-width at half-max) is $1.4'$. The dots show the unit normalized matched filter profile used in the point-source detection algorithm in the ACTPol pixelization of $0.5'$. *Right:* The profile of the high pass filter used to remove large scale modes.

Table 1. Measurements of the polarization fraction of extragalactic sources from selected radio and millimeter wavelength surveys.

Reference	N_{srcs}	Freq (GHz)	Polarization fraction	Remarks
Condon et al. (1998)	30,000	1.4	SS*: 1.1% median, 2% mean SS: 1.8% median, 2.7% mean FS*: 1.3% median, 2% mean	$S_{1.4} > 800$ mJy $200 > S_{1.4} > 100$ mJy
Mesa et al. (2002)	8032 3700 1438 660 6198 2859 1150 496	1.4	SS NVSS sources: 1.82% median SS sources: 1.45% median SS sources: 1.37% median SS sources: 0.74% median FS/IS sources: 1.84% median FS/IS sources: 1.50% median FS/IS sources: 1.32% median FS/IS sources: 1.05% median 2.2% median combined	$200 > S_{1.4} > 100$ mJy $400 > S_{1.4} > 200$ mJy $800 > S_{1.4} > 400$ mJy $S_{1.4} > 800$ mJy $200 > S_{1.4} > 100$ mJy $400 > S_{1.4} > 200$ mJy $800 > S_{1.4} > 400$ mJy $S_{1.4} > 800$ mJy $S_{1.4} > 800$ mJy Anti-correlated with flux density
Klein et al. (2003)	106	2.7, 4.85, 10.5	SS: 2–6%, FS: 2.5% median	1.4–10.5 GHz
Ricci et al. (2004)	197	18.5	FS: 2.7%, SS: 4.8% median	Weakly correlated with $\alpha_{5-18.5}$
Sadler et al. (2006)	108	20	2.3% median	Anti-correlated with flux density
López-Caniego et al. (2009)	138, 122, 93, 81	23, 33, 41, 61	1.7%, 0.91%, 0.68%, 1.3% mean	Bright WMAP sources
Murphy et al. (2010)	768	20	2.6% median, 2.7% mean	FS: 2.9%, SS: 3.8%
Agudo et al. (2010)	149	86	1.5%	Flat-radio-spectrum AGNs
Battye et al. (2011)	105	8.4, 22, 43	2% median, 3.5% mean	Independent of frequency, flux density
Sajina et al. (2011)	159	4.86–43.34 (4 bands)	typically 2–5%, tail extending to ~15%	Slight increase with frequency, trend is stronger for SS and dim sources
Bonavera et al. (2017b)	881	30 44 70 100 143 217 353	3.05% mean 3.27% mean 2.51% mean 3.26% mean 3.06% mean 3.07% mean 3.52% mean	Fractional polarization estimated by applying the stacking technique on 881 sources detected in the 30 GHz Planck map that are outside the Planck Galactic mask
Puglisi et al. (2017)	32	95	FS: 2.07% median	Independent of frequency
Trombetti et al. (2018)	35 9 4 14 15 8 1	30 44 70 100 143 217 353	3.3% median 2.2% median 2.8% median 1.9% median 2.9% median 3.1% median 3.0% median	Independent of frequency, flux density Fractional polarization estimated using the Intensity Distribution Analysis (IDA) method
This work	169	148	2.8±0.5%	Independent of flux density

* SS, FS, and IS denote source populations with steep, flat, and inverted spectrum, respectively.

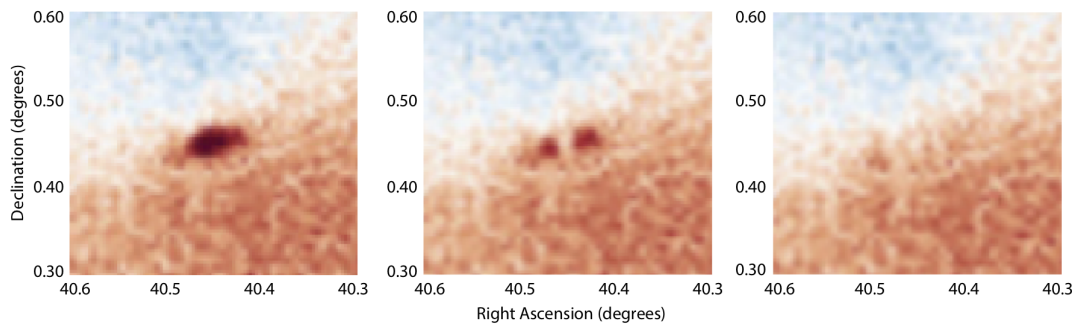


Figure 3. Example of an extended source J024145+002645, the removal of which is accomplished in a two-step matched-filtering method. The left panel shows a thumbnail from the original map, the middle panel shows the residuals after the first run of the source-removal algorithm, and the right panel shows the residuals after applying the source-removal algorithm the second time. The color scale is ± 400 μK .

NRAO Very Large Array - Faint Images of the Radio Sky at Twenty-centimeters (VLA-FIRST) survey (Becker et al. 1995) and the VLA Sky survey (NVSS) (Condon et al. 1998) at 1.4 GHz still provide the most comprehensive catalog of extragalactic radio sources both in total and polarized intensity, mm/sub-mm observations have picked up over the last decade. Table 1 lists a selection of surveys of polarized sources between 1.4 and 353 GHz. All of them have reported low degrees of polarization, on the scale of 1–5%.

SPT (95, 150, 220 GHz); (Vieira et al. 2010; Mocanu et al. 2013) and ACT (148, 218 GHz); (Marriage et al. 2011; Marsden et al. 2014) have reported detection of both synchrotron and dusty sources. More recently, the Planck Early Release Compact Source Catalogue (Planck Collaboration et al. 2011) and subsequent releases of the Planck Catalogue of Compact Sources (Planck Collaboration et al. 2013, 2016) have reported on the properties of sources extracted from all sky maps at nine frequency bands spanning 30–857 GHz. Bonavera et al. (2017a,b) have analyzed the fractional polarization of dusty and radio sources in the Planck maps, respectively, using stacking techniques. Trombetti et al. (2018) have reanalyzed the same using a different approach. However, the polarization properties of extragalactic radio sources still remain poorly constrained at frequencies higher than 20 GHz. Tucci & Toffolatti (2012) and more recently, Galluzzi & Massardi (2016), review the status of radio source observations at radio and mm wavelengths. Casey et al. (2014) reviews the current status of DSFG studies. Massardi et al. (2016) elaborates on the role of radio sources in polarimetric cosmological studies.

The ACTPol receiver deployed on the Atacama Cosmology Telescope (ACT) in Chile has been scanning large areas of the sky with the primary goal of measuring fluctuations in the CMB polarization signal over angular scales up to $\ell \approx 9000$. In this paper, we present the polarization properties of sources detected in the CMB intensity (Stokes I) map made from observations during the first two seasons of the ACTPol survey covering 680 deg² of the sky. We model the distribution of fractional polarization as a function of total source intensity. Extrapolating this model below the ACTPol detection threshold, we predict the impact of the polarized extragalactic source population on our ability to measure the CMB EE power spectrum at high multipoles with future surveys.

This paper is structured as follows. We introduce the ACTPol D56 survey in Section 2. A brief discussion of the source detection in the Stokes I map is provided in Section 3. In Section 4, we present measurements of the polarization fraction of intensity-selected sources in the ACTPol D56 region at 148 GHz from the first two seasons of ACTPol observations. We model the distribution of fractional polarization of the sources as a function of the total source flux density using simulations. In Section 5, we discuss the spectral properties of the ACTPol sources by comparing the measured flux densities with other mm-wavelength and radio surveys. Finally, we predict the impact of the sources on the measurement of the CMB EE power spectrum in Section 6.

2 DATA

2.1 Observations

The Atacama Cosmology Telescope Polarimeter (ACTPol) is a millimeter-wave camera (Thornton et al. 2016) which has surveyed thousands of square degrees of sky with 1.4' resolution and sensitivity to sources at the level of a few milli-Jansky (mJy). Achieving first light in 2013, ACTPol observed in a band centered at 149 GHz (~ 2.0 mm) for the first two seasons. Though the effective central frequency of the broadband receiver to the CMB was 149 GHz, the effective band central frequency of a non-CMB source depends on its spectrum, characterized by spectral indices. These are defined as:

$$\alpha_{\nu_b - \nu_a} = \frac{\log(S_{\nu_a}) - \log(S_{\nu_b})}{\log(\nu_a) - \log(\nu_b)} \quad (1)$$

According to the conventional single power law model, the distribution of source flux densities S as a function of frequency ν is given by $S_\nu \propto \nu^\alpha$. At radio frequencies, a negative α is associated with synchrotron-dominated sources. Sources with free-free as the dominant emission mechanism are characterized by an index close to zero. Sources dominated by graybody re-emission from warm dust, including many of those detected at high redshift, typically have $\alpha > 2$. We follow the method outlined in Appendix A which follows from Page et al. (2003) for computing the effective central frequencies of the broadband ACTPol receiver to sources with different spectra. We do not know the spectral indices of the sources cataloged here, but we assume most are synchrotron dominated. Hence to calculate flux densities, we assume a nominal -0.7 synchrotron index and compute the effective central frequency, 147.6 GHz. We show the results of similar calculations for sources dominated by free-free emission ($\alpha = -0.1$) and dust re-emission ($\alpha = +3.7$) in Appendix A.

In its first season (S13) from September 11, 2013 to December 14, 2013, ACTPol observed four regions of the sky, including the two deep regions D5 and D6 (see Fig. 1), with a single receiver array. In its second season (S14) from August 20, 2014 to December 31, 2014, ACTPol observed two wider regions, one of which was the D56 region which included both the D5 and D6 sub-regions, with two receiver arrays. In this work, we present the properties of extragalactic sources in the night-time data of the wider D56 region including the deeper D5 and D6 sub-regions (Louis et al. 2017) mapped in both S13 and S14. The D56 region covers 680 deg² of the sky with boundaries $-8.8^\circ < \text{Dec} < 5.2^\circ$, $352.0^\circ < \text{RA} < 40.6^\circ$. The D6 region covers 160 deg² with boundaries $-8.4^\circ < \text{Dec} < 0.0^\circ$, $26.0^\circ < \text{RA} < 42.0^\circ$, and the D5 region covers 181 deg² with boundaries $-3.8^\circ < \text{Dec} < 4.8^\circ$, $350.0^\circ < \text{RA} < 4.6^\circ$.

2.2 Maps

The mapmaking procedure is described in Naess et al. (2014) and Dünner et al. (2013). We combine maps made from both arrays and both seasons, inverse-variance weighted by their white noise level. These maps are publicly available on Legacy Archive for Microwave Background Data Analysis

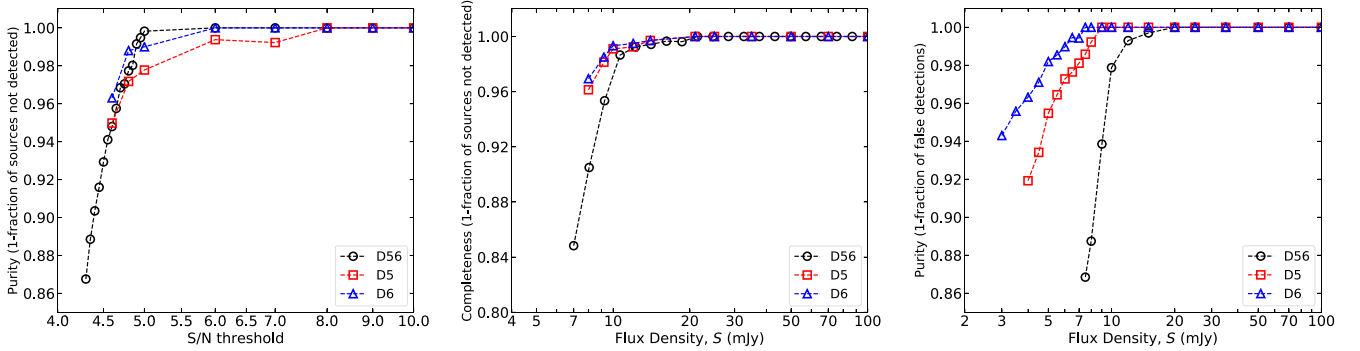


Figure 4. *Left:* Cumulative purity of the catalogs (D56: black, D5: red, D6: blue) as a function of the chosen detection S/N threshold. *Middle:* Cumulative completeness of the catalogs as a function of source flux density. *Right:* Cumulative purity of the catalogs as a function of source flux density. No detections above 20 mJy are expected to be false.

(LAMBDA)¹ and presented in [Louis et al. \(2017\)](#). Combining the S14 data from both arrays for D56, and the S13 data for D5 and D6, the resulting Stokes I map sensitivity is 18, 12, and 11 $\mu\text{K-arcmin}$ for D56, D5, and D6, respectively. The Stokes Q and U sensitivities are the I sensitivities multiplied by a factor of $\sqrt{2}$. The average white noise level, when matched filtered with the ACTPol beam, results in typical sensitivities to point source flux densities of 8 mJy in D56, 4 mJy in D5 and 3 mJy in D6, respectively, with a signal-to-noise ratio (S/N) threshold of 4.5.

3 SOURCE DETECTION

We use the matched filtering method described in [Marriage et al. \(2011\)](#) to detect sources in the intensity map and estimate their amplitudes. Here, we summarize the method and discuss some additional aspects relevant for this work.

We first multiply the map, pixel by pixel, by the square-root of the number of observations per pixel N_{obs} , where an observation represents data acquired over 0.0025 seconds. This accounts for the local variation in the map white-noise level and results in a noise-weighted map with approximately uniform white noise level. The average number of observations per pixel is 5534, and the peak number of observations is 35596. We mask the noisy edges of the survey region, where N_{obs} is below a threshold of 2000; these regions are prone to false detections. The remaining map region is then used for source detection. The matched filter applied to the Fourier transformed map is given by:

$$\Phi_{MF}(\mathbf{k}) = \frac{F_{k_0}(\mathbf{k})\tilde{B}^*(\mathbf{k})|\tilde{T}_{\text{other}}(\mathbf{k})|^{-2}}{\int \tilde{B}^*(\mathbf{k}')F_{k_0}(\mathbf{k}')|\tilde{T}_{\text{other}}(\mathbf{k}')|^{-2}\tilde{B}(\mathbf{k}')d\mathbf{k}'} \quad (2)$$

where \mathbf{k} refers to the wavenumber and $\tilde{B}(\mathbf{k})$ is the Fourier transform of the ACTPol beam. The quantity \tilde{T}_{other} is the Fourier transform of the combination of all expected signal components other than point sources, i.e., atmospheric noise, detector noise, SZ signal, primary CMB, and undetected point sources. The function F_{k_0} represents the same high-pass filter as was used in [Marriage et al. \(2011\)](#), which

tapers off from unity above multipole $\ell = 1200$ to zero at $\ell = 0$ as shown in the right panel of Fig. 2. This is required to remove large scale noise due to the atmosphere. The effective instrument beam ([Louis et al. 2017](#)) is derived from planet and bright point source observations as described in [Hasselfield et al. \(2013\)](#) for the previous generation ACT beam. To arrive at the most accurate and refined representation of the beam, the profiles of the brightest sources in the ACTPol map were examined and fit with the beam profile and a Gaussian broadening term in order to estimate the effect of pointing variance in each region. The azimuthally symmetric beam profile is shown in the left panel of Fig. 2 along with the matched filter profile. A robust estimate of the power spectrum of \tilde{T}_{other} used for this analysis was constructed from the power spectrum of the map itself after masking the brightest sources with $S/N > 50$. This works because the residual source power spectrum is known to be significantly lower than that of the other components.

The source detection proceeds in two steps: first, sources with $S/N > 50$ are identified in an initial run of the source-finder, and masked. This is done to prevent ringing around the very bright sources in the filtered map which could impact detection of the dimmer sources. Next, the matched filter is applied to detect sources with $S/N > 4.5$. The S/N is defined as the temperature at a location in the filtered map divided by the square-root of the variance of the filtered map itself after masking the sources with $S/N > 50$. The finite ACTPol map pixelization of $0.5'$ means that unless a detected source lies exactly at the center of the pixel, the flux estimation would be erroneous. In order to correct for this, we use the method of Fourier interpolation to achieve a finer pixel spacing in map space by a factor of 2^4 as described in [Marriage et al. \(2011\)](#). This enables a more precise estimation of the location of the source peak amplitude after the pixel window function is accounted for. The raw flux densities (in Jy) associated with the source detections are computed from the amplitudes (in μK) following the method described in Appendix A. The flux estimates obtained from the matched filtering method are accurate under the assumption that the sources are intrinsically unresolved. Distant extragalactic sources meet this criterion for ACTPol. However, objects at very low redshifts or with elongated structures, such as highly elliptical galax-

¹ <https://lambda.gsfc.nasa.gov/product/act/>

ies and AGNs with jets or lobes, would appear extended in our maps. The detection and template-based source-removal process does not work well for extended sources. In order to accurately remove these extended sources from the CMB map, we adopt a two-pass detection and removal method. In the first pass, the matched-filter source-finding algorithm is run on the original map and a source catalog is generated. We then subtract a template map (made from this catalog) from the original map and search for residual bright spots (from the initial subtraction) in these template-subtracted maps. We identify nine extended sources using this method. We then run the source-finding algorithm again on a $1^\circ \times 1^\circ$ patch of the template-subtracted map centered around each of these bright spots and perform a second pass of source subtraction. An example is shown in Fig. 3. The total flux for each extended source is obtained by adding together the flux from the two steps.

3.1 Source Catalog

With a S/N threshold of 4.5, 665, 324, and 213 sources were detected in the D56 (S14), D6 (S13), and D5 (S13) regions respectively. The bottom panel of Fig. 1 shows the hit count map of the S14 D56 region used in this work in the background with circles centered at the locations of the sources brighter than 10 mJy. The red circles correspond to sources brighter than 20 mJy. The top left and right panels show similar images for the D6 and D5 regions respectively. Combining the detections in the D56, D5 and D6 maps, 169 sources brighter than 30 mJy in total intensity are selected for the polarization analysis presented in Section 4. This threshold of 30 mJy is chosen because the measurement of polarized flux for dim sources is heavily biased by noise as discussed in Section 4. A catalog of these sources is presented in Table A4 and the full catalog is being released on LAMBDA². The extended sources are marked with an asterisk in the catalog table. The differential source number counts are derived in Section 5.1 separately from two catalogs: the S14 D56 catalog and from the S13+S14 D5+D6 catalog.

3.2 Purity and Completeness of the Source Catalog

The S13+S14 D5 and D6 maps are significantly deeper than the D56 map. In order to estimate the completeness of each of the source catalogs, we inject simulated sources in the source-subtracted original map and run the source detection algorithm on it just as with the original maps. We first generate a catalog of sources with $S/N > 4.5$ by running the source detection algorithm on the original map as described in Section 3. From this catalog, we construct a template map and subtract this from the original map. We then construct a simulated source-only template map the same size as the original map which has 1500 simulated sources at randomly chosen pixels with flux densities down to 5 mJy, drawn from the C2Co model for source counts proposed in Tucci & Toffolatti (2012) (T2012). This map is convolved with the best-fit beam and the resulting map is added to

the source-subtracted map. The source detection algorithm is then run on this map and the resulting catalog is searched for matches to the list of injected sources. The cumulative completeness curve plotted in the middle panel of Fig. 4 shows the fraction of injected sources that were detected above a given flux threshold. Based on this test, the expected completeness of the $S/N > 4.5$ D56 catalog is 87% at 8 mJy, 97% at 10 mJy, and 100% at 20 mJy. The completeness of the $S/N > 4.5$ D5/D6 catalog is 96%/97% at 8 mJy, 99% at 10 mJy, and 100% at 20 mJy. There are no D5/D6 sources with flux greater than 20 mJy in the overlapping area of D56 with D5/D6 that were not also detected in D56. This is consistent with the completeness of the D56 catalog being 100% above 20 mJy.

The number of false detections in each catalog is also estimated from simulations. We start with simulated temperature and polarization maps of the CMB, and add noise to these maps. The noise model is constructed so as to replicate the combined effect of instrumental white noise, atmospheric noise and detector $1/f$ noise in the ACTPol maps. In order to model the noise, we start with “4-way maps” made from four data splits where each split is allocated two consecutive nights of data. The cycle repeats every eight nights. Next, we construct a pair of 2-way maps, each made by co-adding two of the 4-way maps. Then, we compute the noise power spectra from maps obtained by differencing the 2-way maps in I , Q , and U . Noise maps are then constructed given by a Gaussian realization of the noise spectrum of the difference maps. These noise maps are then added to the simulated I , Q and U maps. We then inject sources with flux densities down to 10^{-4} Jy, drawn from the C2Co source counts model, into the simulated I map. The source detection algorithm is then run on this map. We then counted the number of sources detected above a given S/N or flux threshold and look for matches to the list of injected sources. The cumulative purity curves shown in the left and right panels of Fig. 4 plot the quantity $(1 - N_{\text{false}}/N_{\text{total}})$ as a function of the S/N and flux threshold, respectively, where N_{false} is the number of unmatched detections and N_{total} is the total number of detections above the corresponding S/N or flux threshold. The number of false detections in the D56/D5/D6 catalogs are less than 7%/5%/4% for a S/N threshold of 4.5. The expected purity of the $S/N > 4.5$ D56 catalog is thus estimated to be 87% at 8 mJy, 97% at 10 mJy, and 100% at 20 mJy. The expected purity of the $S/N > 4.5$ D5/D6 catalog is estimated to be 94%/98% at 5 mJy, 99%/100% at 8 mJy, and 100% at 10 mJy. We use these estimates of completeness and purity of the catalogs to correct the differential source number counts presented in Section 5.1. There are no D56 sources with flux greater than 20 mJy in the overlapping area of D56 with D5/D6 that were not also detected in the deeper D5/D6 maps. This is consistent with the purity of the D56 catalog being 100% above 20 mJy.

3.3 Deboosting of Source Fluxes

To accurately estimate the intrinsic flux densities of sources given their measured values, we have used a method adapted from Crawford et al. (2010) to correct for the flux boosting effect due to the bias for selecting intrinsically dim sources that coincide with noise fluctuations. We start with the D56 map and subtracted from it a template map constructed

² https://lambda.gsfc.nasa.gov/product/act/actpol_ps_cat_info.cfm

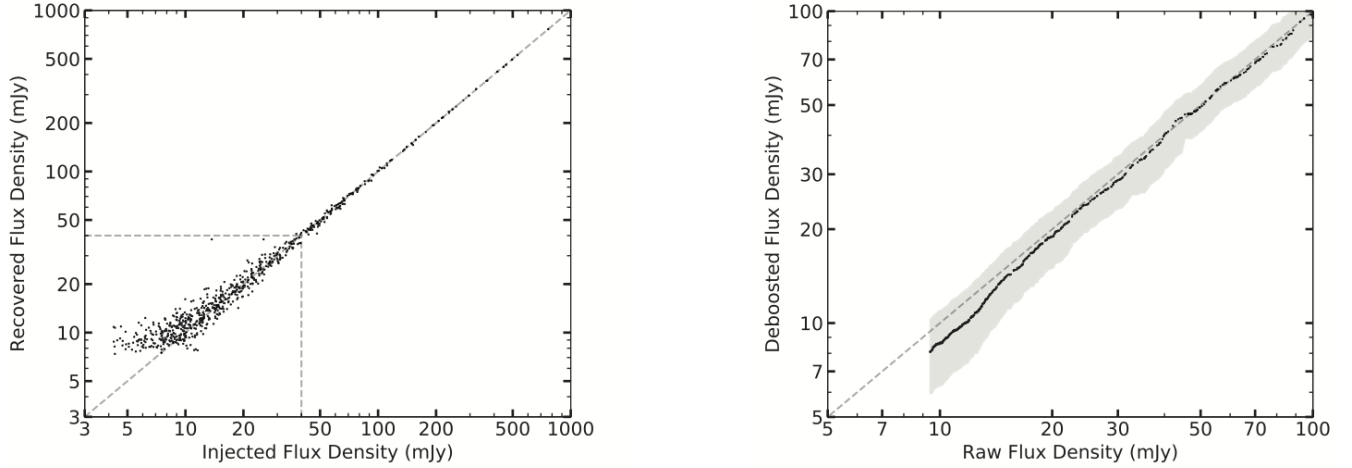


Figure 5. *Left:* Source injection simulations: injected versus recovered source flux densities. The ratio is approximately consistent with unity (dashed line) at the 1% level except for the low flux end ($S < 40$ mJy), where the effect of flux boosting becomes significant. *Right:* Raw versus deboosted source flux densities shown only for sources dimmer than 100 mJy. For e.g., a measured source flux of 10 mJy is deboosted to a true flux of ~ 8.5 mJy. The grey band encompasses the 68% confidence interval derived from the kernel density estimation.

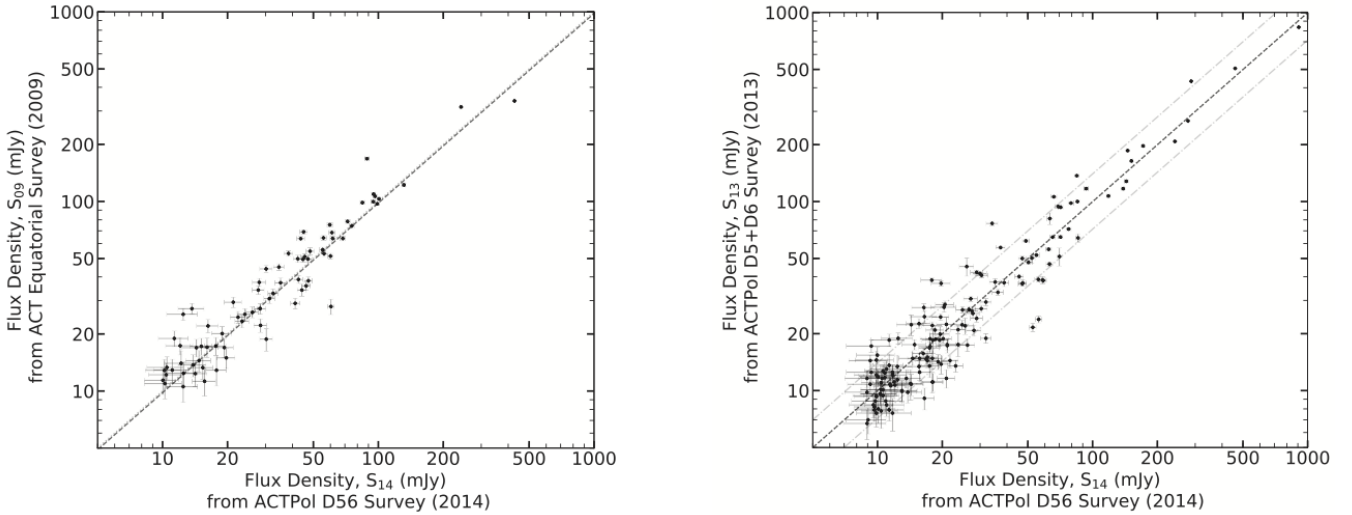


Figure 6. *Left:* Comparison of flux densities of cross-matched sources (with $S_{14} > 10$ mJy) between the ACTPol D56 survey (2014) and the ACT equatorial survey (2009). The dashed line is the best-fit straight line and corresponds to $S_{09} = 0.98 \pm 0.03 S_{14}$ and the dotted line corresponds to $S_{09} = S_{14}$. *Right:* Comparison of flux densities of cross-matched sources (with $S_{14} > 10$ mJy) between the ACTPol D56 survey (2014) and the ACTPol D5 and D6 surveys (2013). The dashed line is the best-fit straight line and corresponds to $S_{13} = 1.00 \pm 0.01 S_{14}$. These sources are predominantly synchrotron and hence expected to be variable with no preference for one direction over another. The fits are forced to pass through zero.

from sources detected down to a S/N threshold of 4. We then populate a zero map the same size as the D56 map with sources at random locations, drawn from the C2Co source counts model, down to a flux threshold of 7 mJy. The C2Co model was selected because it best describes the source counts from this work (see Section 5.1). This map is convolved with the best-fit ACTPol beam and the resulting template map was added to the source-subtracted D56 map. We then run the source finder on this simulated map and verify that the recovered source flux densities are consistent with the injected flux densities at the 1% level (see left panel

of Fig. 5) for sources above a flux density threshold of 40 mJy. Hence, the effect of flux boosting on these sources is expected to be negligible. While selecting the lower flux limit for the injected sources, we chose a flux cut of 7 mJy that is sufficiently lower than the dimmest source whose flux we are trying to deboost, i.e., 10 mJy; this is done to minimize the effect of incompleteness in the low flux end.

Using this simulated map, we extract the true underlying posterior probability distribution $\mathcal{P}(S_{\text{max}}|S_{\text{p,m}})$ for the intrinsic flux density of the brightest source within a pixel

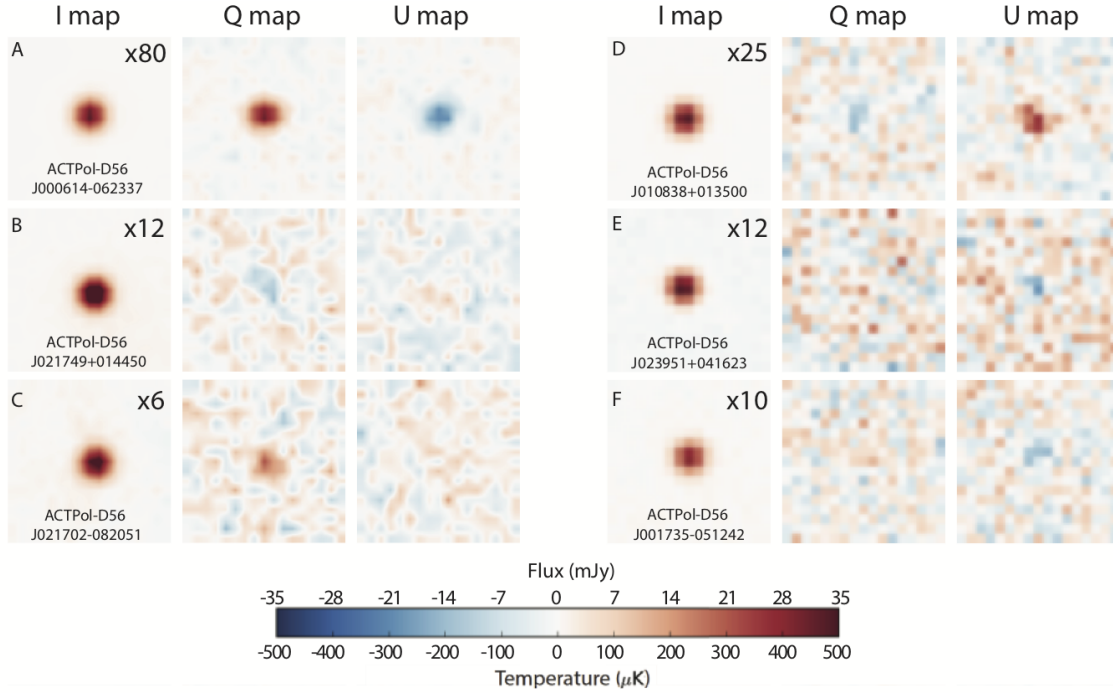


Figure 7. I , Q , and U thumbnails (0.02 deg^2 in area) of six intensity-selected sources that have the strongest signal in polarization. The intensity map temperatures have been scaled down by a factor noted in the top right corner of the I thumbnails so as to keep the color scale same for I , Q , and U . The color scale spans $\pm 500 \text{ } \mu\text{K}$ for all but the brightest source in the top left panel ($\pm 2000 \text{ } \mu\text{K}$).

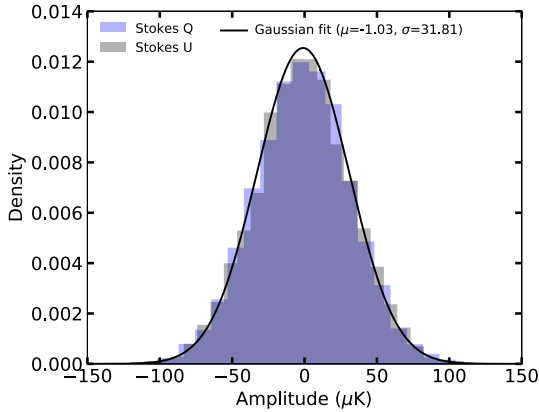


Figure 8. Histograms of pixel values for the Stokes Q (purple) and U (grey) D56 maps. The black line is a Gaussian with mean equal to the average of the Q and U values and standard deviation equal to the average of the σ_Q and σ_U values.

as:

$$\mathcal{P}(S_{\text{max}}|S_{\text{p},m}) \propto \mathcal{P}(S_{\text{p},m}|S_{\text{max}})\mathcal{P}(S_{\text{max}}) \quad (3)$$

where $S_{\text{p},m}$ is the measured source flux in a pixel, and $\mathcal{P}(S_{\text{p},m}|S_{\text{max}})$ is the likelihood of measuring flux $S_{\text{p},m}$ in a pixel given the brightest source in that pixel has flux S_{max} . The prior $\mathcal{P}(S_{\text{max}})$ is given by:

$$\mathcal{P}(S_{\text{max}}) \propto \frac{dN}{dS} \exp\left(-\Delta\Omega_p \int_{S_{\text{max}}}^{\infty} \frac{dN}{dS'} dS'\right) \quad (4)$$

where $\Delta\Omega_p$ is the solid angle corresponding to each pixel. The effect of the dN/dS source count distribution is essentially

implemented in the simulations by drawing sources from the C2Co dN/dS model. In order to compute the posterior given by equation (3) for each detection with measured flux $S_{\text{p},m}$, we started by noting each source detected in the simulated map with flux in the range $0.85 S_{\text{p},m}$ to $1.15 S_{\text{p},m}$. We find every matching injected source (within a matching radius of 0.01°), and compare the recovered and injected flux densities. We then apply a kernel density estimator (KDE) to the distribution of injected source flux densities. The bandwidth parameter for the KDE is chosen to be $0.15 S_{\text{p},m}$. The true, underlying posterior $\mathcal{P}(S_{\text{max}}|S_{\text{p},m})$ for a measured flux $S_{\text{p},m}$ is then simply obtained by normalizing the resulting probability density distribution multiplied by the exponential term in equation (4). The right panel of Fig. 5 shows the deboosted flux densities plotted against the raw measured flux densities for sources detected with total flux less than 100 mJy . As expected, the correction due to deboosting becomes more significant for dimmer sources. We report the deboosted flux densities for sources with measured total flux below 100 mJy in Table A4.

3.4 Source Variability

The majority of the sources in this study are synchrotron dominated, presumably AGN-powered radio galaxies. These are likely to be variable, attributable to the birth and expansion of new components and shocks forming in relativistic flows in parsec-scale regions. The variations may be on times scales of hours to months or even years. We examine variability of the sources treated here by cross-matching with the ACT equatorial catalog (Gralla et al. 2018) composed of sources observed in 2009. The left panel of Fig. 6 shows

a comparison of the measured flux densities between 2009 and 2014. The best fit straight line through these points has a slope of 0.98 ± 0.03 . We also compare measured flux densities of 158 sources observed both during the 2013 (D5+D6) and 2014 (D56) seasons of ACTPol observations in the right panel of Fig. 6. The best fit straight line through these points has a slope of 1.00 ± 0.01 . The slope of the best fit line being close to unity in both comparisons implies that on average, there is no bias introduced by source variability or calibration of our data across seasons. In other words, there is no preference of the flux densities to vary in one direction over another, on average. On the other hand, the obvious scatter about the best fit line seen in the form of a significant number of data points lying well away from the unity slope line is an indication of source variability. A detailed study of source variability across seasons of ACTPol observations is underway and will be the topic of a future paper. Comparing the measured per-season flux densities of the 158 sources observed during both seasons, we find 36 sources with flux densities varying by more than 40% between the two seasons. These are the data points lying outside the two dash-dot lines in Fig. 6 and are flagged as variable in the catalog table.

4 FRACTIONAL POLARIZATION OF INTENSITY-SELECTED SOURCES

While hundreds of sources are detected in the total intensity map, the situation is very different in the case of the polarization maps, where only eight sources are detected with signal-to-noise ratio greater than 5. Fig. 7 shows thumbnails of six sources having the strongest signal in polarization. We investigate the polarization properties of the 169 intensity-selected sources in the D56 map brighter than 30 mJy in total flux density. Polarization is quantified with the Stokes Q and U components:

$$\begin{aligned} Q &= pI \cos(2\psi), \\ U &= pI \sin(2\psi) \end{aligned} \quad (5)$$

The polarization fraction, p , and polarization angle, ψ , can then be derived as:

$$\begin{aligned} p &= \sqrt{q^2 + u^2}, \text{ where } q = \frac{Q}{I}, \text{ and } u = \frac{U}{I} \\ \psi &= \frac{1}{2} \arctan(U/Q) \end{aligned} \quad (6)$$

The estimates of the Stokes parameters from the D56 Q and U maps are unbiased and approximately uncorrelated, but computing the polarized flux introduces a noise bias because of the squaring, which is significant when the signal-to-noise ratio is low. In the presence of measurement noise, a hypothetical source with a true polarization fraction $p_0 = 0$ can appear to have a $p > 0$, unless the noise bias is accurately subtracted. This bias was first discussed in [Serkowski \(1958\)](#) and has since been treated extensively in the literature: [Simmons & Stewart \(1985\)](#) account for the biases when Stokes parameters are uncorrelated and have the same errors; an analytic, approximate distribution of p for the general case of correlated errors was developed by [Plaszczynski et al. \(2014\)](#); [Quinn \(2012\)](#) and [Maier et al. \(2014\)](#) adopted a Bayesian approach based on the assumption of Gaussian

error; [López-Caraballo et al. \(2011\)](#), [Rubio-Martín et al. \(2012\)](#), and [Stil et al. \(2014\)](#) corrected for polarization bias through a Monte Carlo analysis; and [Montier et al. \(2015a,b\)](#) compared several estimation methods. This paper takes a new approach of using maps with uncorrelated noise constructed from data splits to avoid the noise bias. Our goal is to estimate the true values I_0 , Q_0 , and U_0 of the Stokes parameters, given measured values I , Q , and U . The fundamental assumption we make is that the measurements of I , Q , and U are described by a three-dimensional Gaussian with standard deviations σ_I , σ_Q , and σ_U , respectively. Fig. 8 shows the noise distribution for Stokes Q and U maps, where sources detected in total intensity are masked out of the Q and U maps leaving pixels that are free of detectable polarized emission. We then use our source finding algorithm to pick out the Q and U amplitudes at 10^4 randomly selected locations on the maps, just as we would do for extracting the Q and U amplitudes of the intensity-selected sources. We calculate the average Q , U , σ_Q , and σ_U values to be -1.03 , -1.03 , 31.8 , and $31.9 \mu\text{K}$, respectively. The solid curve in Fig. 8 represents a Gaussian distribution with mean equal to the average of the Q and U values and standard deviation equal to the average of the σ_Q and σ_U values. This describes well the Q and U probability density functions and thus validates our assumption. We get the measured value for the total intensity I and the uncertainty in its measurement σ_I from the matched filtering method as described in Section 3. The Stokes Q and U measurements for these intensity-selected sources and their respective uncertainties σ_Q and σ_U are then obtained using the same matched filtering method on the Q and U maps at the locations of the detections in the I map.

4.1 Systematics: Temperature-to-Polarization leakage

We consider the simplest of a range of systematic effects that can lead to power from the Stokes I map contaminating the Stokes Q and U maps. As we are dealing with faint polarization signals, it is essential to correct for any such I-to-P leakage. An approximate estimate of this instrument-induced systematic effect is obtained by performing a combined fit of the $Q(U)$ pixel values at each location of the detections in the I map to the inverse variance weighted average $Q(U)$ value plus a variable temperature leakage term $\alpha_{I-Q}I$ ($\alpha_{I-U}I$). The 336 sources with total flux between 10 and 20 mJy were used for this fitting. The percentage leakages are found to be $\alpha_{(I-Q)} = 0.13 \pm 0.15\%$ and $\alpha_{(I-U)} = 0.24 \pm 0.16\%$ and are corrected for in the calculation of the polarized flux.

4.2 Noise Bias Corrected Fractional Polarization

In the presence of random noise, the distribution of the degree of linear polarization can be approximated by a Gaussian only for sources with a strong Q or U signal. In the measurement of the fractional polarization p , for a source with an intrinsic fractional polarization p_0 , the statistical distribution of noise is a Rice distribution ([Serkowski 1958](#)):

$$F(p; p_0, \sigma_p) = \frac{p}{\sigma_p^2} J_0 \left(i \frac{p p_0}{\sigma_p^2} \right) \exp \left(-\frac{p^2 + p_0^2}{2\sigma_p^2} \right) \quad (7)$$

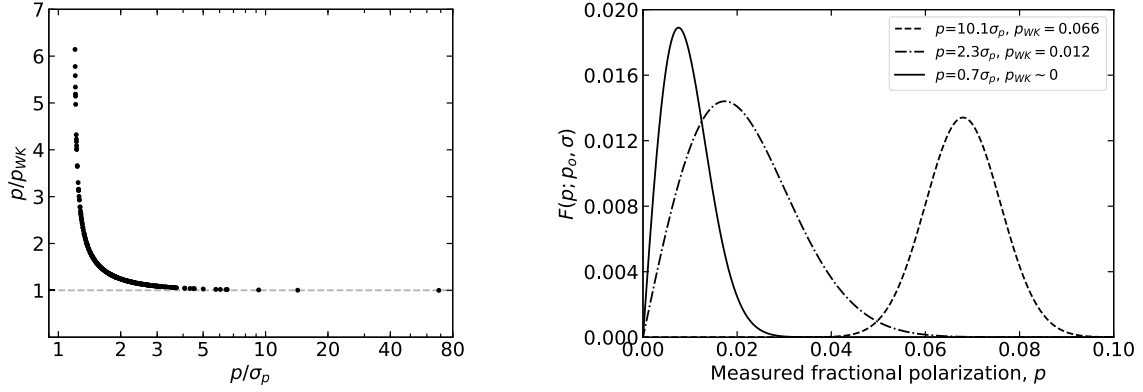


Figure 9. *Left:* Ratio of measured p to the noise bias removed estimate, p_{WK} as a function of p/σ_p . For high values of p/σ_p , p_{WK} approaches p and as p approaches σ_p , p_{WK} approaches zero. *Right:* Rice distribution for the measured p of three example sources with $p = 0.7\sigma_p$, $p = 2.3\sigma_p$, and $p = 10.1\sigma_p$. The peak of the distribution corresponds to the most probable observed value of p . Here p_{WK} is the noise bias subtracted estimate of the intrinsic fractional polarization.

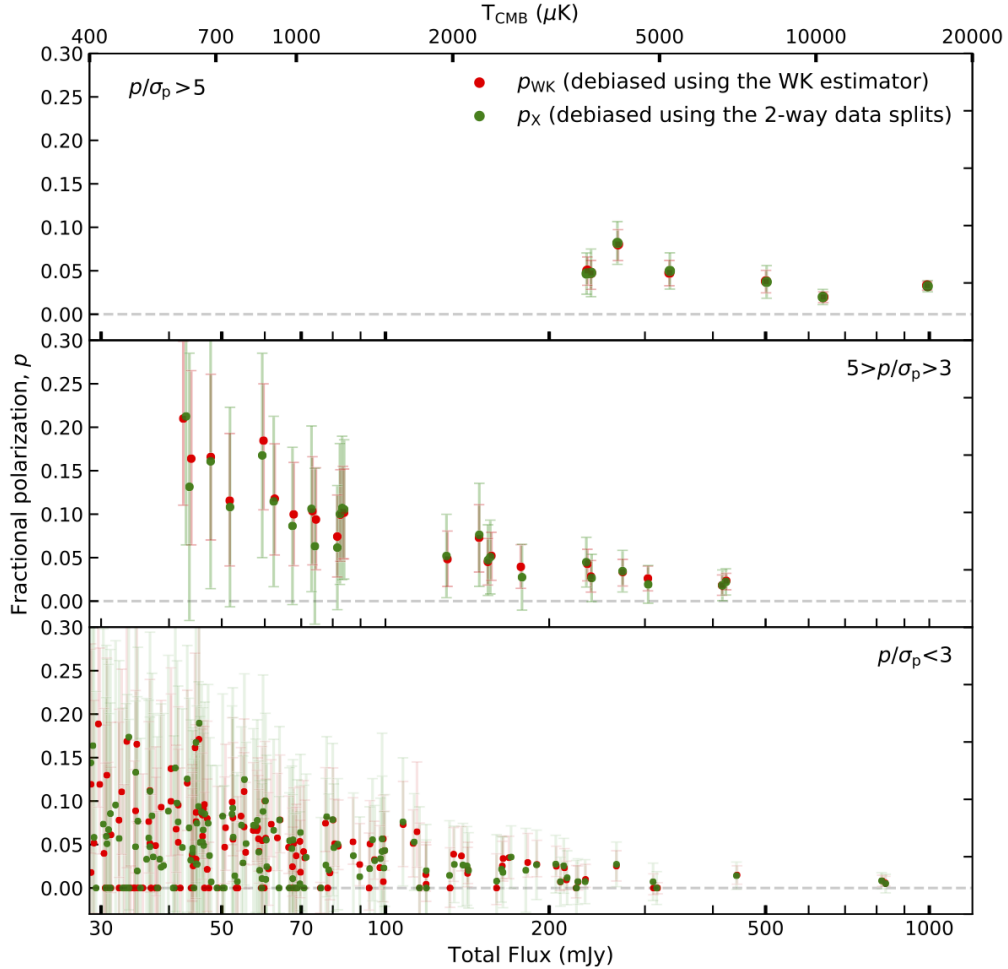


Figure 10. Measurements of fractional polarization plotted against total flux density. The raw measurements are debiased using (a) the Wardle-Kronberg estimator (red), and (b) 2-way data splits (green). *Top:* Sources detected in polarization with $p > 5\sigma_p$. The error bars represent the 95% confidence interval. *Middle:* Sources with $5\sigma_p > p > 3\sigma_p$. *Bottom:* Sources with $p < 3\sigma_p$. The green error bars are uncertainties in estimates of p obtained using method (b), where each of the 2-way maps contains only half the data, and hence the error bars are larger. The green data points at $p = 0$ correspond to sources for which the quantity $q_1 q_2 + u_1 u_2$ is negative.

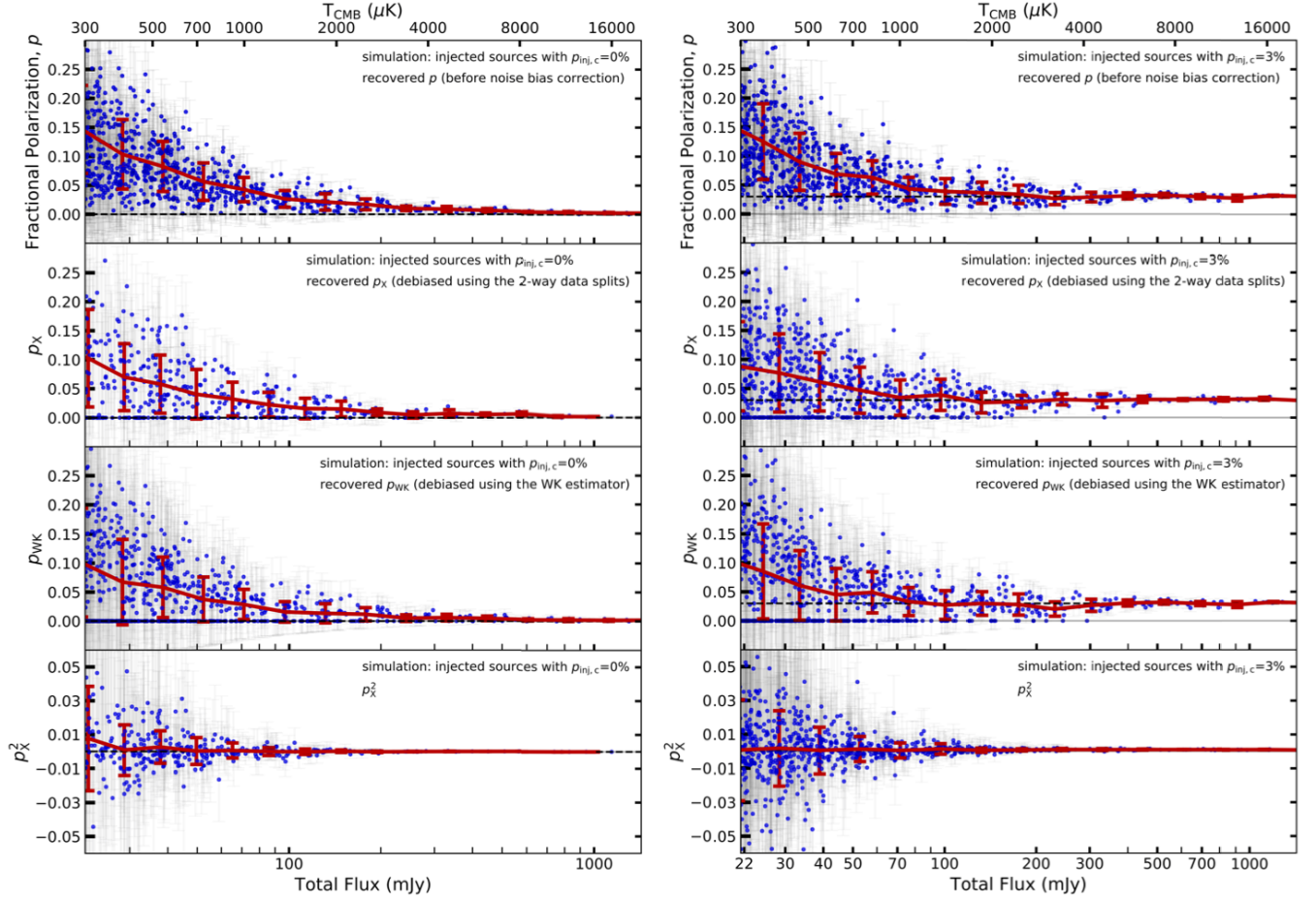


Figure 11. “C” simulations: injected sources with a constant polarization fraction, $p_{\text{inj},c} = 0$ (left) and 0.03 (right). The polarization angles of the sources are randomly drawn from a flat distribution. The blue dots represent the polarization fractions of the injected sources recovered from the simulated maps along with the 95% confidence intervals and the red lines connect the average fractional polarization values binned in total intensity with the error bars denoting the 1σ standard deviation $\sigma_{p_{\text{rec},c}}$ within each bin. The apparent lack of data points near $p = 0$ at the low flux end in the top left panel is a consequence of the noise bias which is significant at the low flux end and biases the recovered p away from zero. The residual bias in the recovered p from the 2-way maps at low total flux comes from the fact that p is only defined if p^2 is positive. The plot of p^2 versus total flux from the 2-way maps shows that the de-biasing works well on average. (continued in Fig. 12)

where the uncertainty, $\sigma_p \approx \sigma_q \approx \sigma_u$, and $\sigma_{q,u} = \sigma_{Q,U}/I$. Fig. 9 shows the Rice distribution $F(p; p_o, \sigma_p)$ for three sources: one each with $p < \sigma_p$, $p > \sigma_p$, and $p \gg \sigma_p$. For sources with $p \gg \sigma_p$, the Rice distribution is close to Gaussian, and $p_o \approx p$. Simmons & Stewart (1985) have critiqued and compared various methods for noise bias correction and shown that all of them leave some residual bias, especially when p/σ_p is small. They further showed that the method developed by Wardle & Kronberg (1974) is one of the most effective in removing noise bias from measurements of fractional polarization of point sources. We perform the noise bias correction in two ways: using the Wardle-Kronberg (which we will call “WK”) estimator and using 2-way maps (defined in Section 3.2) constructed from 4-way data splits.

The “WK” estimator is defined as the value of the intrinsic fractional polarization \hat{p}_{WK} , for which the observed value p is equal to the maximum of the Rice distribution. This is obtained by solving the equation that we get by differentiating equation (7) with respect to p and setting it to

zero as below.

$$J_0\left(i\frac{p\hat{p}_{\text{WK}}}{\sigma_p^2}\right)\left(1 - \frac{p^2}{\sigma_p^2}\right) - i\frac{p\hat{p}_{\text{WK}}}{\sigma_p^2}J_1\left(i\frac{p\hat{p}_{\text{WK}}}{\sigma_p^2}\right) = 0 \quad (8)$$

We obtain the noise bias corrected value of the source fractional polarization p_{WK} as:

$$\begin{aligned} p_{\text{WK}} &= \hat{p}_{\text{WK}} \text{ when } p < 4\sigma_p, \text{ and} \\ p_{\text{WK}} &= \sqrt{p^2 - \sigma_p^2} \text{ when } p > 4\sigma_p \end{aligned} \quad (9)$$

It follows from equation (8) that for any measured value p less than or equal to σ_p , the intrinsic fractional polarization p_{WK} is equal to zero. Fig. 9 shows a plot of the ratio p/p_{WK} as a function of p/σ_p , where p_{WK} approaches 0 as p/σ_p approaches 1. The 95% upper and lower confidence interval limits on the estimate of p_{WK} for any measured p is obtained using the Rice distribution as the probability density function of the estimator. Given the shape of the Rice dis-

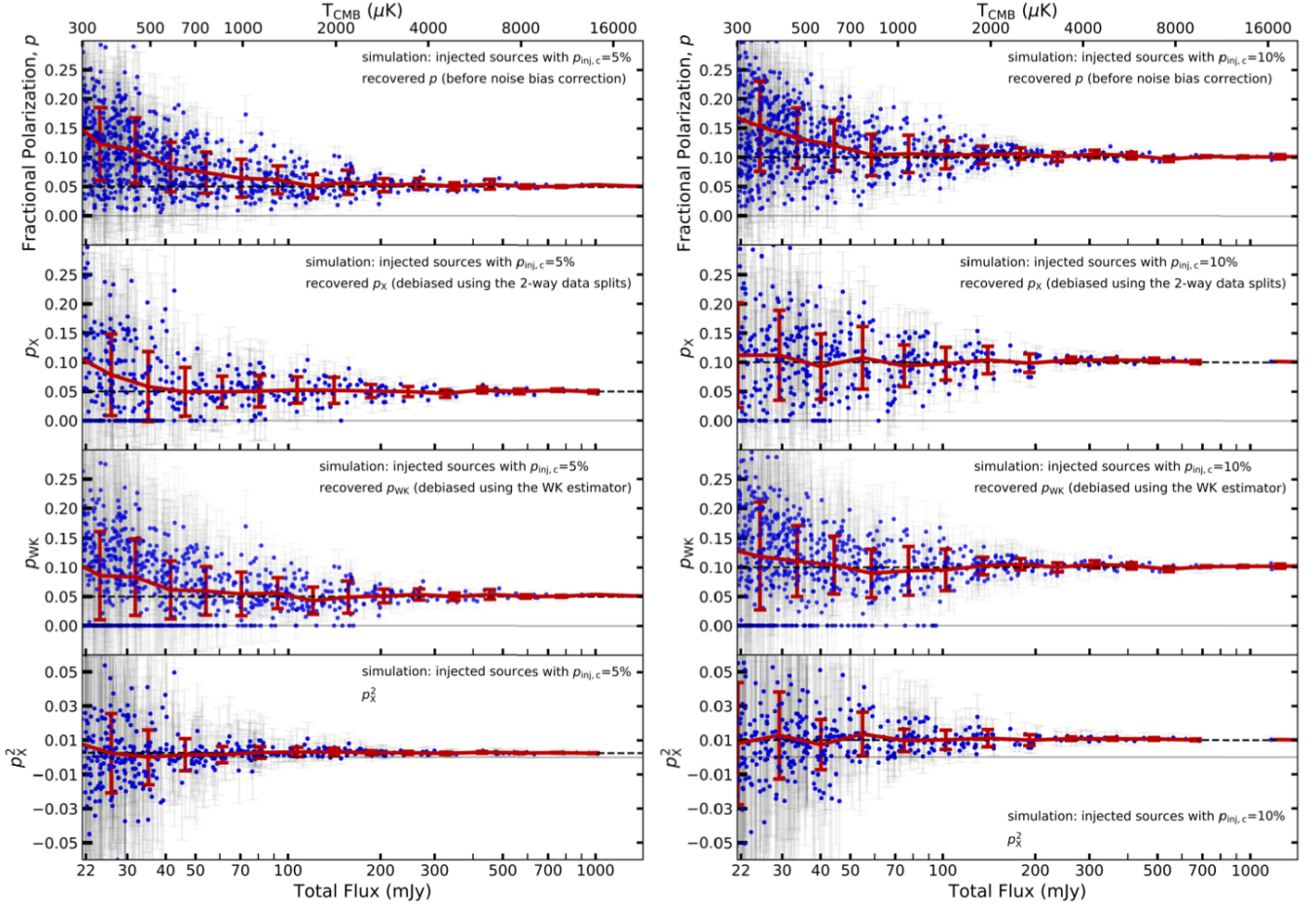


Figure 12. (continued from Fig. 11) “C” simulations: injected sources with a constant polarization fraction, $p_{\text{inj},c} = 0.05$ (left) and 0.10 (right). The polarization angles of the sources are randomly drawn from a flat distribution. The blue dots represent the polarization fractions of the injected sources recovered from the simulated maps along with the 95% confidence intervals and the red lines connect the average fractional polarization values binned in total intensity with the error bars denoting the 1σ standard deviation $\sigma_{p_{\text{rec},c}}$ within each bin. The residual bias in the recovered p from the 2-way maps at low total flux comes from the fact that p is only defined if p^2 is positive. The plot of p^2 versus total flux from the 2-way maps shows that the de-biasing works well on average.

tribution, these error bars are asymmetric in general, except when $p \gg \sigma_p$.

In the second method, we use the 2-way maps with uncorrelated noise to naturally de-bias the measurement of p . We get the amplitudes of the Stokes I , Q , and U at the locations of the intensity-selected sources independently from the two maps. Then, the intrinsic fractional polarization p_x is computed as below.

$$p_x = \sqrt{q_1 q_2 + u_1 u_2} \quad (10)$$

where $q_{1,2} = Q_{1,2}/I_{1,2}$ and $u_{1,2} = U_{1,2}/I_{1,2}$. If the quantity under the square root $q_1 q_2 + u_1 u_2$ is negative, the Q and U amplitudes could be attributed to random fluctuations and we set p_x equal to zero. This method naturally de-biases the measurement of p .

Informed by simulations described in Section 4.3 below, we trust the accuracy of the de-biasing method when the total flux density of a source is greater than 215 mJy ($\sim 2900 \mu\text{K}$). We have significant detection, defined by $p > 3\sigma_p$, of the polarization signal in 14 out of 26 such sources shown in

the center ($5 > p/\sigma_p > 3$) and top ($p/\sigma_p > 5$) panels of Fig. 10 with error bars that encompass the 95% confidence interval. The red points represent measurements of fractional polarization de-biased using the first method, and green points correspond to estimates obtained using the second method. For sources with $p < 3\sigma_p$, we show the estimates of their fractional polarization in the bottom panel of Fig. 10. The errors on the estimate of p_x are larger than the errors on the estimate of p_{WK} because the Q and U errors are larger when using half the data as in the case of the 2-way maps compared to the full map. The error in the measurement of each source polarization fraction is obtained from a thousand realizations of Gaussian distributed Q_1 , Q_2 , U_1 , U_2 , I_1 , and I_2 about the measured values giving a distribution for p_x^2 . The 95% confidence interval for p_x^2 is then obtained from a kernel density estimator applied to the distribution of p_x^2 . The errors are then propagated to errors on p_x . Table A4 reports the fractional polarization of sources brighter than 74 mJy ($\sim 1000 \mu\text{K}$) in total intensity, de-biased using the two methods. It should be noted however, that for the

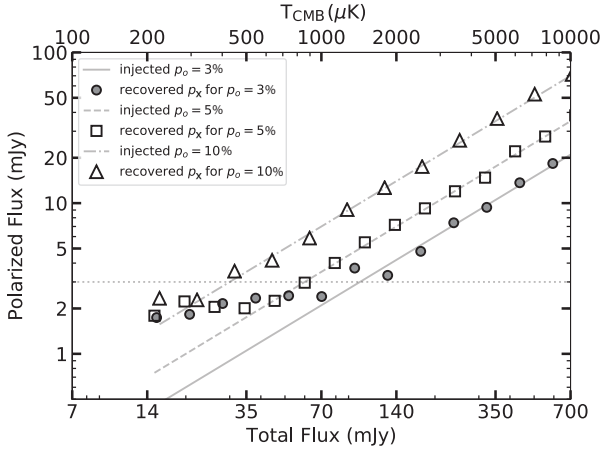


Figure 13. The binned average values of the recovered polarized flux as a function of the total flux for injected source populations having constant $p_o = 0.03$ (circle), 0.05 (square), 0.10 (triangle). The measured polarized flux values were de-biased using the 2-way maps and this plot shows that the de-biasing works well when the polarized flux $P \gtrsim 3$ mJy as evident from the fact that the recovered values shown by the dots follow the injected values shown by continuous lines, but diverge for $P \lesssim 3$ mJy indicating residual bias.

sources with total flux density between 74 and 215 mJy, the reported p_{WK} , p_{X} values could potentially be overestimates, as discussed below.

4.3 Simulations

Simulations of the measured quantities are used to statistically analyze the calculated fractional polarization and any residual bias after our noise-bias removal. First, sources detected in total intensity down to a flux density level of 5 mJy are masked out of the D56 Stokes I , Q and U maps. We again create a template map the same size as the D56 map where all pixels are set to zero. Random pixels are selected from this template map and assigned amplitudes drawn from the C2Co source counts model down to a flux level of 5 mJy. We call this the total intensity template map for simulated sources. Each source is assigned a known polarization fraction and a random polarization angle and the corresponding Q and U amplitudes are computed. With these, similar template maps are created for Q and U . These three template maps are then convolved with the ACTPol beam and added to the source subtracted I , Q , and U maps respectively. We then take these maps with simulated sources and estimate the polarization fractions for the sources in the same way as for the real maps. We run multiple realizations for a few different hypothetical source populations which we refer to as “C” (see Figs. 11–12) for sources with a constant polarization fraction $p_{\text{inj},c}$, and “tG” (see Fig. 14) for sources that are assigned a polarization fraction drawn from a Gaussian distribution with mean $p_{\text{inj},tG}$ and standard deviation $\sigma_{p_{\text{inj},tG}}$ truncated at $p_{\text{inj},tG} = 0$ (see Figs. 11–14). We compare the two methods for noise bias correction and find that both methods work well for estimating the average polarization properties of a source population when either I_{inj} is greater than ~ 215 mJy or both p_{inj} is greater than 3% and the polar-

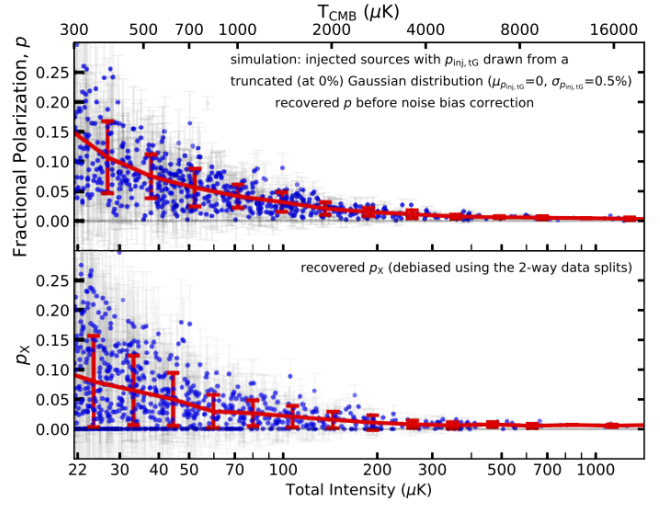


Figure 14. “tG” simulations: injected sources that are assigned a polarization fraction drawn from a Gaussian distribution with mean $\mu_{p_{\text{inj},tG}} = 0$ and standard deviation $\sigma_{p_{\text{inj},tG}} = 0.005$. The polarization angles of these sources are randomly drawn from a flat distribution. The blue dots represent the polarization fractions of the injected sources recovered from the simulated maps along with the 95% confidence intervals and the red lines connect the average fractional polarization values binned in total intensity with the error bars denoting the 1σ standard deviation $\sigma_{p_{\text{rec},tG}}$ within each bin.

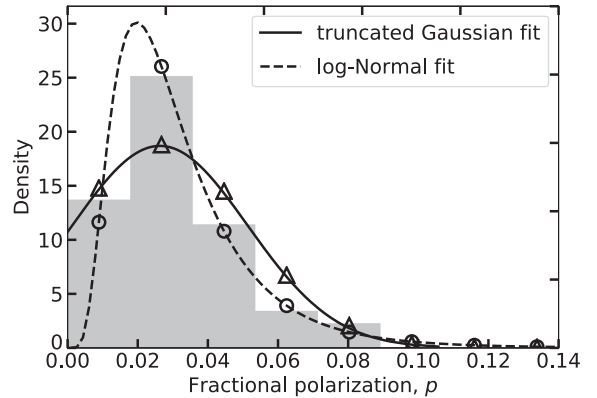


Figure 15. Histogram of the measured fractional polarization p_{X} for sources detected with total flux density $S > 30$ mJy and having a non-zero p_{X} . The dashed line shows the best-fit log-normal distribution to this data described by $\mu_{\text{LN}} = 0.027$ and $\sigma_{\text{LN}} = 0.572$ and the solid line shows the best-fit truncated Gaussian distribution with $\mu_{p,tG} = 0.027$ and $\sigma_{p,tG} = 0.025$.

ized flux given by $P_{\text{inj}} = p_{\text{inj}} I_{\text{inj}}$ is greater than ~ 3 mJy. When $P < 3$ mJy, both methods leave a residual bias as shown in Fig. 13. We consider our measurement of the fractional polarization of individual sources to be unbiased only for the 26 sources with total flux density above 215 mJy.

4.4 Distribution of Fractional Polarization

In addition to measuring the polarization of the extragalactic point sources, we predict the distribution of their po-

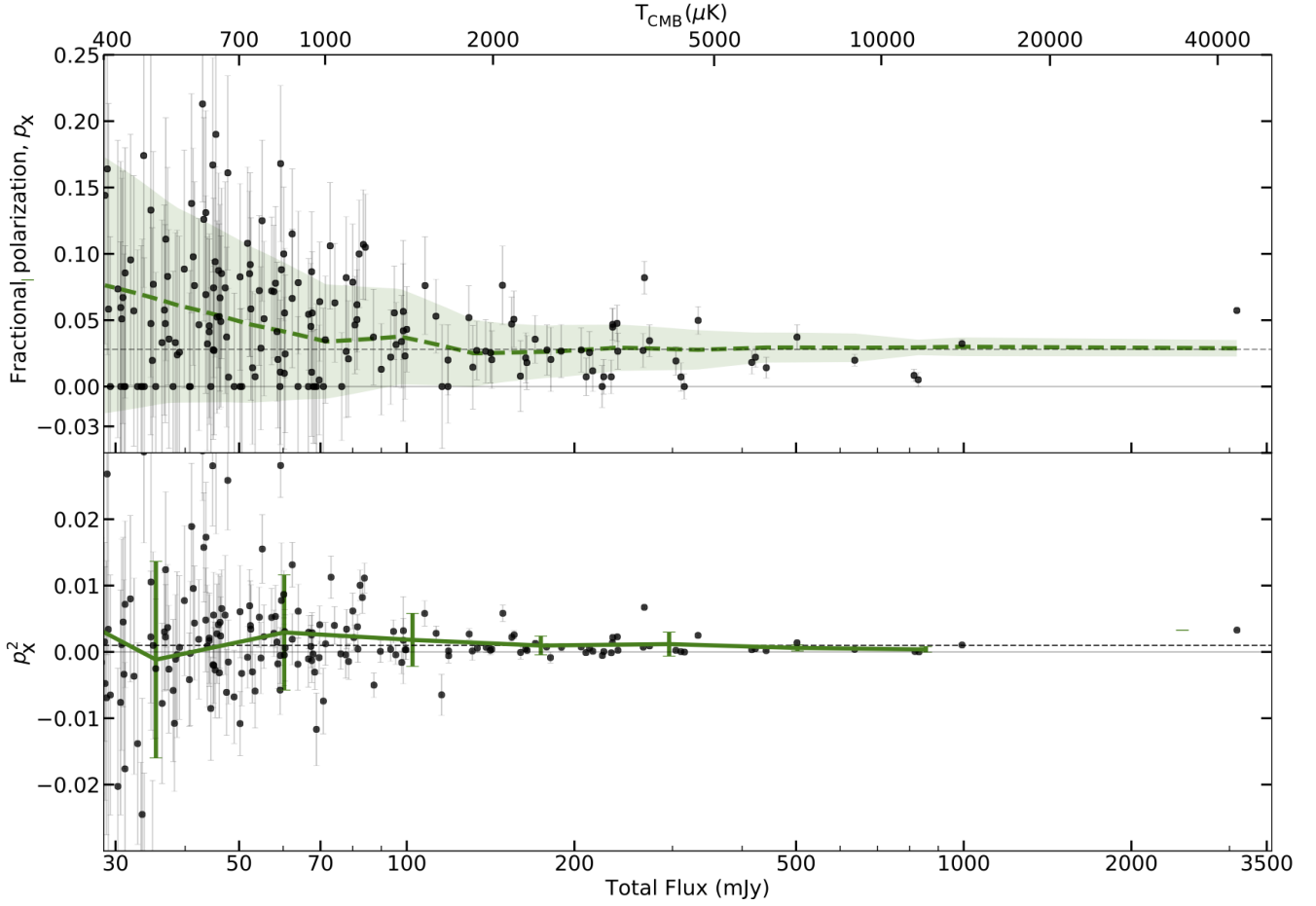


Figure 16. *Top:* The green dashed line ($p = 0.028$) shows the best fit model for the distribution of fractional polarization with the green band representing the $\pm 1\sigma_{\text{pm}}$ ($\sigma_{\text{pm}} = 0.054$) uncertainty band. The data points represent sources with total intensity above $410 \mu\text{K}$ or total flux density above 30 mJy that were used in the fitting with individual error bars representing the 68% confidence interval. The data points at $p = 0$ correspond to sources for which the quantity $q_1 q_2 + u_1 u_2$ is negative. The gray lines are at $p = 0$ (solid) and 0.028 (dashed). *Bottom:* Distribution of $p^2 = q_1 q_2 + u_1 u_2$ from the 2-way maps as a function of total flux. The green line shows the data binned in total intensity with the error bars denoting the 1σ standard deviation. The grey dashed line corresponds to $p^2 = 0.028^2$.

larization fraction as a function of total intensity that is valid not only down to the sensitivity level of the D56 map but also extendable to lower flux limits. This helps predict the contribution of unsubtracted point sources to the E-mode polarization power spectrum at high- ℓ . Earlier work by Mesa et al. (2002) and Tucci et al. (2004) presented fractional polarization distributions for NVSS sources, exhibiting a log-normal form. They further concluded that NVSS sources exhibited an anti-correlation between fractional polarization and total flux as did 1.4 GHz polarimetric studies of the ELAIS-N1 field by Taylor et al. (2007), Grant et al. (2010), and ATLAS fields by Subrahmanyan et al. (2010). However, Hales et al. (2014) argued that this apparent anti-correlation represented a selection bias. Since it is very hard to detect low levels of fractional polarization for the faint sources in total intensity, the average fractional polarization of detected polarized sources will always appear to increase with decreasing total flux. Hales et al. (2014) also found the distribution to be log-normal and that the maximum level of fractional polarization exhibited by ATLAS sources was not

correlated with total flux density. Bonavera et al. (2017b) implemented a stacking technique to estimate the average fractional polarization from 30 to 353 GHz of a primary sample of 1560 compact sources detected in the 30 GHz Planck all-sky map (Planck Collaboration et al. 2016) and described the distribution of fractional polarization as log-normal and independent of frequency. Trombetti et al. (2018) extract polarization degrees of radio sources from measurements of signals in a map at the positions of a given source catalog and comparing with that for the blank sky, measured at random positions, away from sources. They find a median fractional polarization of 2.83% across the Planck frequencies 30–353 GHz. Puglisi et al. (2017) present a compendium of previous polarization measurements and using a log-normal fit to the distribution of polarization fractions, they show that most experiments are consistent with a level of polarization around 1–5% largely independent of frequency. Our data is consistent with this level of polarization as described below. In order to model the distribution of the fractional polarization p of the AGN source population, we use simulations

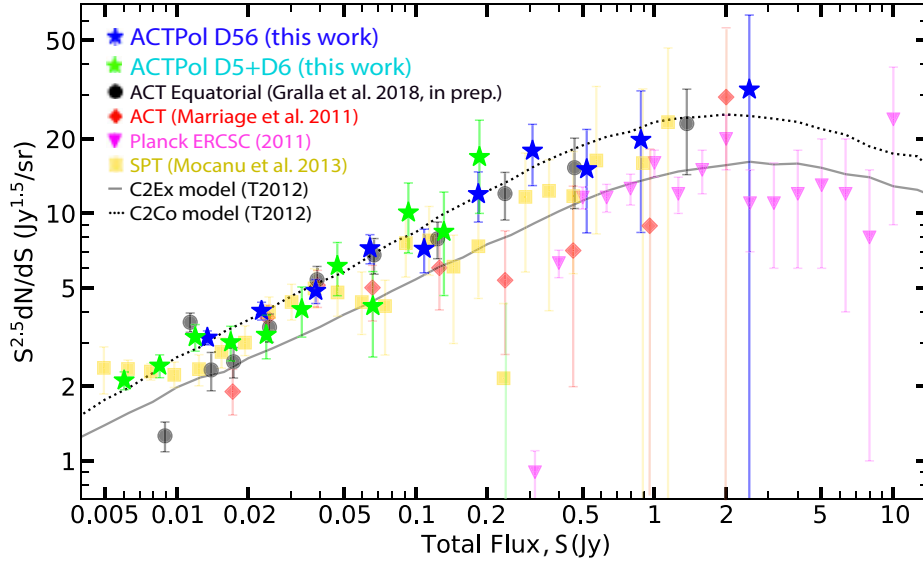


Figure 17. Differential Source Number Counts in Total intensity. The ACTPol 148 GHz differential source number counts (corrected for incompleteness and purity, D56: blue stars, D5+D6: green stars) are plotted together with measurements from the ACT equatorial survey (Gralla et al. 2018) at 148 GHz (black circles), ACT southern survey (Marriage et al. 2011) at 148 GHz (red diamonds), Planck ERCSC (Planck Collaboration et al. 2011) at 143 GHz (magenta triangles), SPT (Mocanu et al. 2013) at 148 GHz (gold squares), and the T2012 C2Ex model (solid gray line) and C2Co model (dotted black line) for radio and infrared source populations at 143 GHz. The error bars on the measurements are Poissonian.

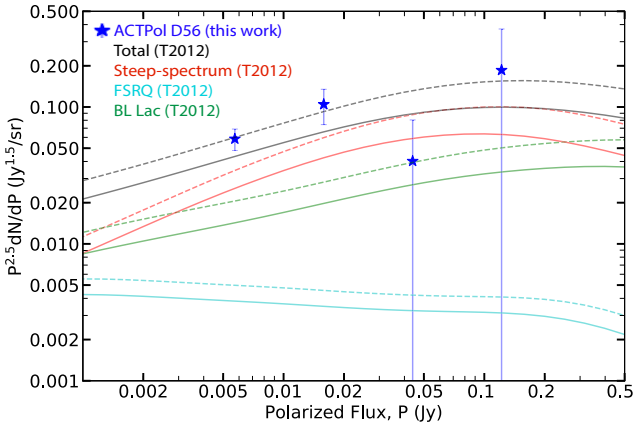


Figure 18. Differential Source Number Counts in Polarized intensity. Comparison of the measured ACTPol source number counts with predictions from T2012 for different source populations: the solid lines represent their “optimistic” model and the dashed lines represent their “conservative” model. The error bars on the measurements are Poissonian.

to statistically analyze the measured distribution of p as a function of intensity. Battye et al. (2011) argued that the distribution of fractional polarization p could be modeled as a Gaussian in $\log(p)$. In other words, the probability density function would follow a log-normal distribution (T2012) given by:

$$f(p; \mu_{\text{IN}}, \sigma_{\text{IN}}) = \frac{1}{p\sqrt{2\pi\sigma_{\text{IN}}^2}} \exp\left[-\frac{(\ln(p/\mu_{\text{IN}}))^2}{2\sigma_{\text{IN}}^2}\right] \quad (11)$$

where we fit for the values of μ_{IN} and σ_{IN} , the mean and the standard deviation in log, respectively. One can then obtain a good approximation of the fractional polarization using a combination of the log-normal parameters as:

$$\begin{aligned} \langle p_{\text{IN}} \rangle &\approx \mu_{\text{IN}} e^{\frac{1}{2}\sigma_{\text{IN}}^2} \\ \langle p_{\text{IN}}^2 \rangle &\approx \mu_{\text{IN}}^2 e^{2\sigma_{\text{IN}}^2} \\ p_{\text{IN,med}} &\approx \mu_{\text{IN}} \end{aligned} \quad (12)$$

Fig. 15 shows a comparison of the best-fit log-normal distribution with parameters $\mu_{\text{IN}} = 0.027$ and $\sigma_{\text{IN}} = 0.572$ and the best-fit truncated Gaussian distribution with $\mu_{p,\text{tG}} = 0.027$ and $\sigma_{p,\text{tG}} = 0.025$ along with a histogram of the measured fractional polarization p_x for sources detected with total flux density $S > 30$ mJy and having a non-zero p_x . Both the fits have a χ^2 per degree of freedom less than 1 and seem to describe our observations well. The estimates for $\langle p_{\text{IN}} \rangle$, $\langle p_{\text{IN}}^2 \rangle^{1/2}$, and $p_{\text{IN,med}}$ from the log-normal parameters are 0.032, 0.038, and 0.027 respectively. In this work, we choose a truncated Gaussian model to describe our observed fractional polarization because it appears to capture the sources with very low measured levels of polarization better than the log-normal distribution.

We use the method described in Section 4.2 to recover the fractional polarization of injected sources from the “C” and “tG” simulations. The results for a few of these simulations are shown in Figs. 11, 12, and 14. These simulations are then interpolated over values between $p_{\text{inj,c}} = 0$ and 0.10 and $\sigma_{p_{\text{inj,tG}}} = 0.005$ and 0.10. Our model source population consists of a constant polarization fraction component $p_{\text{m,c}}$, and a variance $\sigma_{p_{\text{m}}}^2$ as model parameters. While only the “tG” simulations have a standard deviation $\sigma_{p_{\text{inj,tG}}}$ as a simulated parameter, both simulations have a variance in the

distribution of the data points corresponding to the recovered p values (see Figs. 11, 12, and 14). The model parameter $\sigma_{p_m}^2$ is the sum of these data space variances $\sigma_{p_{rec,c}}^2$ and $\sigma_{p_{rec,IG}}^2$ following the convention of adding uncorrelated errors in quadrature. The best fit to the measured fractional polarization is determined by optimizing over the parameters $p_{m,c}$ and $\sigma_{p_m}^2$ to minimize the χ^2 as given by equation (13). Since $\sigma_{p_m}^2$ is a free parameter in our fits, we can lower the χ^2 of our fit by increasing $\sigma_{p_m}^2$ indefinitely, and hence we decide to stop when a χ^2 of unity is reached.

$$\chi^2 = \frac{1}{n} \sum_{i=1}^n \left(\frac{p_{meas,i} - p_{m,i}}{\sigma_{p_{m,i}}} \right)^2 \quad (13)$$

where, $p_{m,i} = p_{inj,c,i}$

and, $\sigma_{p_{m,i}} = \sqrt{\sigma_{p_{rec,IG,i}}^2 + \sigma_{p_{rec,c,i}}^2}$

We are essentially fitting for the intrinsic scatter in the fractional polarization of the source population we are investigating. We perform the fitting with sources whose total flux is greater than 30 mJy and measurement of p de-biased using the 2-way maps. The best fit model is described by $p_{m,c} = 0.028 \pm 0.005$ (where the quoted uncertainty is the standard error on the mean) and $\sigma_{p_m} = 0.054$, the $\pm 1\sigma_{p_m}$ error band is shown in the top panel of Fig. 16. This value of the mean fractional polarization is consistent with the best-fit value in Fig. 15 and with $p_m = 0.027 \pm 0.004$ for the 26 sources with total flux density greater than 215 mJy, whose estimates of fractional polarization are expected to be free of residual noise bias. Hence our findings are consistent with the scenario that the fractional polarization of the radio source population we are probing is independent of total intensity or total flux density down to the limits of our measurements. Our estimate for the average fractional polarization is consistent with the numbers typically in the range 1–5% reported by other mm-wave and radio surveys listed in Table 1. Deeper maps at 148 GHz together with maps at five frequencies spanning 24–280 GHz from subsequent seasons of the ACTPol and Advanced ACTPol (AdvACT) surveys will significantly improve the statistics on the polarization properties of extragalactic sources at millimeter wavelengths.

5 COMPARISON TO OTHER SOURCE CATALOGS

5.1 Differential source number counts

The differential source number counts per steradian in total intensity dN/dS from the ACTPol two-season catalogs are shown in Fig. 17 along with counts from other surveys at similar frequencies. The data are presented in Table 5.1. The number counts are plotted separately for the S14 D56 and the S13+S14 D5+D6 maps, the latter being much deeper. For flux densities lower than 40 mJy, the ACTPol counts shown are deboosted and corrected for incompleteness and expected number of false detections. We compare our counts to the T2012 C2Ex and C2Co models, which are constructed based on extrapolations of number counts from high radio frequencies (5 GHz) and observed counts from SPT (Vieira

et al. 2010; Mocanu et al. 2013) and ACT (Marriage et al. 2011), building on the earlier models proposed in de Zotti et al. (2005). These models consider the spectral behavior of the different source populations, flat-spectrum (FSRQs and BL Lac), steep-spectrum and inverted spectrum, in a statistical way and feature different distributions of spectral break frequencies for FSRQs and BL Lacs, and the effects of spectral steepening. Tucci & Toffolatti (2012) found that the C2Ex model was the best fit to then available observational counts above 100 GHz. Both the ACTPol (this work) and the ACT equatorial (Gralla et al. 2018) counts favor the C2Co model over the C2Ex model favored by the Planck counts (Planck Collaboration et al. 2011) at 148 and 220 GHz for sources above 500 mJy. The reduced χ^2 of the fit of the C2Ex and C2Co models to our D56/(D5+D6) counts is 5.0/1.9 and 2.8/0.4, respectively. Mocanu et al. (2013) reported that the C2Ex model is a good fit to the SPT counts above 80 mJy and below 20 mJy in all bands (95, 150, and 220 GHz), but under-predicts the counts in the intermediate flux range at 95 and 150 GHz.

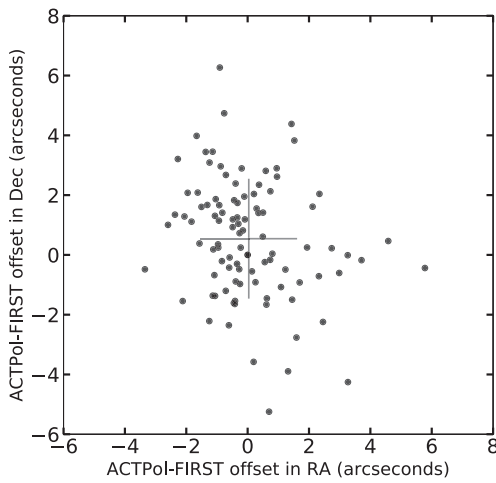
The differential number counts per steradian in polarized intensity dN/dP as a function of the polarized flux P are compared with the T2012 models for different source populations in Fig. 18. Sources detected in total intensity with S/N greater than 5 and total flux density greater than 74 mJy with noise-debiased polarized flux greater than 3 mJy were included to derive the dN/dP here. Tucci & Toffolatti (2012) proposed two models (a “conservative” case and an “optimistic” case) for each source population. They also reported that for observational counts at frequencies below 40 GHz, the “optimistic” model is a good fit, especially when the polarized flux P is below 50 mJy, whereas the “conservative” model fits the observational counts well at high polarized fluxes. Based on this work, we find that the “conservative” model for all source populations combined fits our data only marginally better with a reduced χ^2 of 1.3 compared to 1.4 for the “optimistic” model, shown in Fig. 18. More polarization data are required to better constrain the dN/dP models.

5.2 Astrometry

The accuracy of the absolute positions of the sources in the catalog is checked by cross-matching against radio sources listed in the Very Large Array - Faint Images of the Radio Sky at Twenty-centimeters (VLA-FIRST) survey (Becker et al. 1995), in which the astrometry of the maps is accurate to $0.05''$, and individual sources at the 3 mJy level have 90% confidence error circles of radius less than $0.5''$. We compare the positions of 99 of the brightest ($S > 50$ mJy) sources detected in the D56 intensity map to positions of sources in the VLA-FIRST catalog within a search radius of $10''$. The distribution of the positional offsets in right ascension (RA) and declination (Dec) are shown in Fig. 19. The errorbars are centered on the mean offsets, and extend as far as the 1σ standard deviation (rms) of the offsets. The mean offsets in RA and Dec are $0.04 \pm 0.16''$ and $0.54 \pm 0.20''$ respectively (where the quoted uncertainty is the standard error on the mean, i.e., σ/\sqrt{N} , where $N = 99$). The rms offset in RA and Dec are $1.55''$ and $1.98''$ respectively. The rms astrometry

Table 2. Completeness and purity corrected differential source number counts at 148 GHz for synchrotron-dominated AGN population

D5+D6:	Total Flux	D56:	Total Flux	D56:	Polarized Flux
Tot Flux, S (mJy)	$S^{2.5} dN/dS$ (Jy ^{1.5} sr ⁻¹)	Tot Flux, S (mJy)	$S^{2.5} dN/dS$ (Jy ^{1.5} sr ⁻¹)	Pol Flux, P (mJy)	$P^{2.5} dN/dP$ (Jy ^{1.5} sr ⁻¹)
5.0–7.1	2.1±0.2	10.0–16.9	3.2±0.2	3.4–9.5	0.06±0.01
7.1–9.9	2.4±0.3	16.9–28.5	4.0±0.3	9.5–26.4	0.10±0.03
9.9–14.0	3.2±0.4	28.5–48.0	4.9±0.5	26.4–73.2	0.04±0.04
14.0–19.7	3.0±0.5	48.0–80.9	7.2±1.0	73.2–203	0.19±0.19
19.7–27.8	3.2±0.7	80.9–136	7.2±1.4		
27.8–39.1	4.1±0.9	136–230	12.0±2.8		
39.1–55.1	6.1±1.5	230–388	17.9±5.0		
55.1–77.5	4.2±1.6	388–654	15.1±6.8		
77.5–109	10.1±3.2	654–1102	19.8±11.4		
109–154	8.4±3.8	1858–3132	31.7±31.7		
154–217	16.9±6.9				

**Figure 19.** Positional offsets between the ACTPol D56 catalog and the VLA-FIRST catalog obtained by comparing the positions of 99 ACTPol sources detected with flux greater than 50 mJy and their VLA-FIRST counterparts. The cross is centered on the mean ACTPol-FIRST offset (0.04'', 0.54'') with lengths along either axis indicating the rms offset (1.55'', 1.98'').

error is thus consistent with zero pointing offset in RA and a less than 1'' pointing offset in Dec.

5.3 Cross-matching with other catalogs

We cross-match the D56 sources with catalogs from observations at other frequencies. Matches are established within a given radius about a source. The radius is chosen based on the predicted positional errors of the catalog being cross-matched with, the beam size of the instruments, and by looking at the distribution of offsets between D56 sources and their closest counterpart in each catalog. We consider the following catalogs from surveys that overlap with the D56 region: NVSS and VLA-FIRST at 1.4 GHz, AT20G at 20 GHz, ACT Equatorial at 148, 218, and 277 GHz, and Herschel SPIRE at 600 and 1199 GHz.

NVSS at 1.4 GHz: The National Radio Astronomy Observatory (NRAO) Very Large Array (VLA) Sky Survey, also known as NVSS, covers the sky north of declination -40° at 1.4 GHz. The NVSS catalog consists of almost 2 mil-

lion discrete sources (Condon et al. 1998) brighter than a flux threshold of about 2.5 mJy observed between Sep 1993 and Oct 1996 with a resolution of 17.5''. The root mean square uncertainties in RA and Dec vary from $\leq 1''$ for the 400,000 sources stronger than 15 mJy to 7'' at the survey limit. The catalog also reports measurements of the polarized flux. Among the 103 D56 sources brighter than 50 mJy, 97 matches are found in the NVSS catalog within a matching radius of 10''. We find 456 matches for the 493 D56 sources with deboosted flux greater than 10 mJy within a matching radius of 15''. Based on tests of the catalog purity, less than 15 false detections with flux greater than 10 mJy are expected in the D56 catalog.

VLA-FIRST at 1.4 GHz: The VLA-FIRST survey (Becker et al. 1995). Data for the FIRST survey were collected from Spring 1993 through Spring 2004 using an elliptical beam with an approximate $6.5'' \times 5.4''$ FWHM. The astrometry of the maps is accurate to 0.05'', and individual sources have 90% confidence error circles of radius $< 0.5''$ at the 3 mJy level. The catalog contains close to a million sources. Among the 103 D56 sources brighter than 50 mJy, 99 matches are found in the VLA-FIRST catalog within a matching radius of 10''. We find 470 (317) matches for the 493 (337) D56 sources with deboosted flux greater than 10 (15) mJy within a matching radius of 15''. The right panel of Fig. 20 shows the 1.4 (VLA) – 148 (ACTPol) GHz source spectral indices plotted against the measured 148 GHz flux density. The four D56 sources brighter than 50 mJy with no matches in either VLA-FIRST or NVSS are ACTPol-D56 J005735–012334 (an extended source), J233757–023057, J021921–025842, and J010643–031536. Of these, only J233757–023057 has a match in the Herschel SPIRE 600 and 1199 GHz catalogs.

AT20G at 20 GHz: The Australia Telescope 20 GHz Survey (AT20G) is a blind radio survey carried out at 20 GHz with the Australia Telescope Compact Array (ATCA) from 2004 to 2008, and covers the whole sky south of Dec 0° . The AT20G source catalog described in Murphy et al. (2010) includes 5890 sources above a flux-density limit of 40 mJy. All AT20G sources have total intensity and polarization measured at 20 GHz. The declination band $0^\circ > \text{Dec} > -15^\circ$ was observed during Aug-Sep 2007 with an approximate beam size of 30''. Out of 381 D56 sources south of declination 0° that are brighter than 10 mJy, 137 matches were found within 10'' and 147 within 30'' in the AT20G

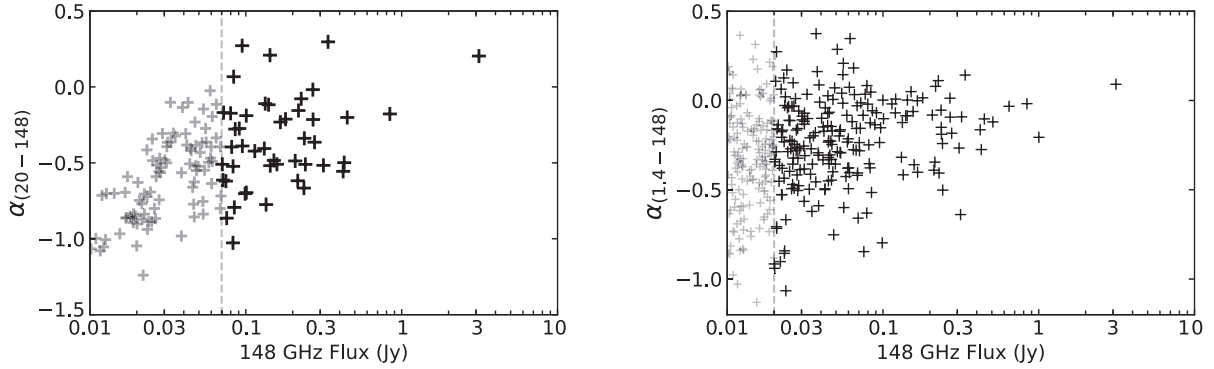


Figure 20. Spectral indices between 20–148 GHz (left) and 1.4–148 GHz (right) plotted against measured total flux at 148 GHz for ACTPol-AT20G and ACTPol-VLA FIRST cross-identified sources with 148 GHz flux density greater than 10 mJy. The black pluses represent sources brighter than 70 mJy (left) and 20 mJy (right) at 148 GHz. In the left panel, the vertical gray dashed line is at $S_{148} = 70$ mJy, below which the data suffers from a selection bias owing to the incompleteness of the AT20G catalog that excludes sources with flat or peaked spectra. In the right panel, the vertical gray dashed line is at $S_{148} = 20$ mJy, below which the 148 GHz ACTPol data is incomplete.

catalog. All of the 46 D56 sources brighter than 70 mJy were cross-identified within AT20G sources within a search radius of $10''$. Of these 46 sources in the AT20G catalog, 15 have polarization measurements and 20 sources have upper limits on their polarization. The left panel of Fig. 20 shows the 20 (AT20G) – 148 (ACTPol) GHz source spectral indices plotted against the measured 148 GHz flux density. The low flux density ($S_{148} < 70$ mJy) data suffers from a selection bias owing to the incompleteness of the AT20G catalog that excludes sources with flat or peaked spectra. The sources with $S_{148} > 70$ mJy represent a complete sample.

ACT Equatorial Survey at 148, 218, and 277 GHz: ACT conducted surveys of the equatorial sky from 2007 to 2010, observing at three frequencies simultaneously: 148 GHz (~ 2.0 mm), 218 GHz (~ 1.4 mm) and 277 GHz (~ 1.1 mm) with angular resolutions of $1.4'$, $1.0'$, and $0.9'$, respectively. The point source catalog from this survey (Gralla et al. 2018) includes 148 and 218 GHz data from the 2009 and 2010 observing seasons, and 277 GHz data from the 2010 observing season. We find 87 cross-matched sources (see Fig. 6) in the overlapping region between D56 and the ACT equatorial survey that are detected in all three ACT frequency bands by the multifrequency matched filter method described in Gralla et al. (2018). Of these, only five (marked with a \dagger symbol in Table 5.3, see below) have dusty spectra identified by $\alpha_{148-217} > 1.0$ in Gralla et al. (2018). Of these, two sources J024145+002645 (an extended source, see Fig. 3) and J020941+001549 have counterparts in the 1.4 GHz NVSS catalog. Dusty sources can have a strong synchrotron component from electrons accelerated in supernovae, the so-called IR-radio correlation (Helou et al. 1985). The FIRST counterpart could be associated with this synchrotron emission.

Herschel SPIRE at 600 and 1199 GHz: The Spectral and Photometric Imaging Receiver (SPIRE) instrument on-board Herschel mapped about 9% of the sky at 250, 350, and 500 μm (1199, 857, and 600 GHz) with spatial resolutions of $17.9''$, $24.2''$ and $35.4''$, respectively. The SPIRE 1199 and 600 GHz catalogs (Schulz 2017) consist of nearly a million and two hundred thousand objects, respectively.

Among the 493 D56 sources brighter than 10 mJy, 32 and 28 matches are found in the SPIRE 1199 and 600 GHz catalogs within a radius of $10''$. Table 5.3 lists potential DSFG candidates detected at 148 GHz in the D56 intensity map with $S/N > 4$ and $S_{148} > 10$ mJy with counterparts in the non-contemporaneous SPIRE 250 μm or 500 μm catalogs and $\alpha_{148-600} \gtrsim 1.0$ or $\alpha_{148-1199} \gtrsim 1.0$. The brightest of these sources is J020941+001549 which is a gravitationally lensed hyperluminous infrared radio galaxy at redshift $z = 2.553$ (Geach et al. 2015); it does not have a detectable polarization signal at 148 GHz. The next brightest source is the extended source J024145+002645; its measured polarization fraction at 148 GHz is $2.8^{+4.9}_{-3.8}\%$. The ACTPol-SPIRE cross-matched sources were cross-checked with the SDSS image database³. Some of these sources were found to be nearby galaxies and were excluded from the table. Contemporaneous multi-frequency AdvACT data will throw more light on the spectra of these sources.

5.4 Spectral Energy Distribution and Color-color diagram

Spectral energy distributions (SEDs) and color-color comparison of spectral indices have been widely used to classify sources based on their dominant emission mechanisms (Murphy et al. 2010). The ACTPol 148 GHz catalog is dominated by synchrotron-dominated blazars, which have variable flux densities, often not periodic. Hence, the inferred spectrum of a given source will depend on the epoch of observation, although not biased one way or the other. Here, we are deriving spectral indices from AT20G, VLA-FIRST, and ACTPol surveys which are not contemporaneous, which complicates things further. However, treating the catalog as a whole, a spectral study may give rise to insights about the average spectral behavior of the source population being probed.

³ <http://skyserver.sdss.org/dr14/en/tools/chart/listinfo.aspx>

Table 3. Potential DSFG candidates detected in the ACTPol 148 GHz two-season map and cross-matched in the Herschel SPIRE catalogs. Spectral indices in the table are computed using flux values at 1.4, 600, and 1199 GHz from NVSS, SPIRE 500 μm , and SPIRE 250 μm catalogs, respectively, but from observations that are not contemporaneous with the ACTPol D56 survey. The blank entries correspond to no cross-matches. The sources marked with a \dagger symbol have dusty spectra identified by $\alpha_{148-217} > 1.0$ in Gralla and those marked with a $*$ symbol are described in further detail there.

ID ACTPol-D56	RA hh:mm:ss	Dec deg:min:sec	S/N	S_{148} mJy	$\alpha_{1.4}^{148}$	α_{148}^{600}	α_{148}^{1199}
J004533-000115 †*	00:45:32.7	-00:01:15.0	5.4	10.8		1.5	
J005950-073436	00:59:49.9	-07:34:36.3	8.9	17.5	-0.4	2.7	
J011248-001721 †	01:12:48.3	-00:17:20.6	6.8	13.9	-0.1	1.3	1.7
J011255+005904 †	01:12:54.6	+00:59:03.9	5.4	10.2		2.1	
J011531-005147 †	01:15:30.9	-00:51:47.0	5.1	10.3		2.1	1.7
J020941+001549 †*	02:09:41.0	+00:15:48.8	8.6	15.1	0.3	2.8	2.0

Sources detected at 148 GHz with $S/N > 4$ and $S_{148} < 10$ mJy and with counterparts in the SPIRE 500 μm or 250 μm catalogs

ID ACTPol-D56	RA hh:mm:ss	Dec deg:min:sec	S/N	S_{148} mJy	$\alpha_{1.4}^{148}$	α_{148}^{600}	α_{148}^{1199}
J000202-010457	00:02:02.4	-01:04:56.5	4.1	8.7	-0.2		0.9
J000553-050604	00:05:52.7	-05:06:03.6	4.3	8.3		1.4	1.2
J002116+013314	00:21:15.8	+01:33:13.8	4.4	8.1		1.6	
J003253-034445	00:32:53.0	-03:44:45.2	4.1	8.4		1.5	1.2
J003815-002254 $*$	00:38:14.5	-00:22:54.4	4.0	8.1		2.0	1.2
J021402-004625	02:14:02.2	-00:46:24.5	5.4	3.8		2.5	1.6
J021830-053144	02:18:30.1	-05:31:44.0	6.6	4.3		2.5	1.5
J021941-025535	02:19:40.7	-02:55:34.6	4.7	3.0			1.0
J022422-044455	02:24:21.9	-04:44:55.2	4.9	3.2			1.2
J022552-045028	02:25:52.1	-04:50:28.2	4.6	3.1			1.0
J022946-034102	02:29:45.6	-03:41:01.6	4.7	3.2			1.6
J233426-042514	23:34:26.0	-04:25:13.9	4.0	8.4		1.4	
J234051-041930	23:40:50.7	-04:19:29.8	4.8	9.4		2.2	1.4

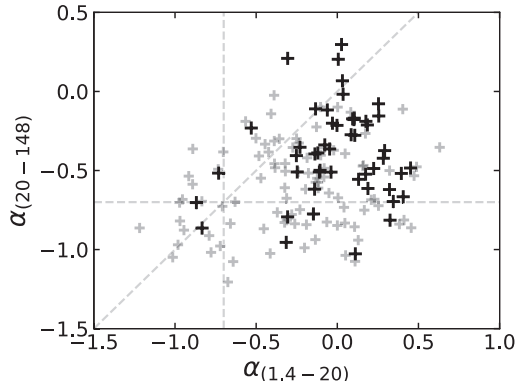


Figure 21. Color-color diagram: 1.4–20 GHz spectral indices are plotted against 20–148 GHz spectral indices for 148 ACTPol-AT20G-VLA FIRST cross-identified sources with measured total flux at 148 GHz greater than 20 mJy. The black pluses represent sources that are brighter than 70 mJy at 148 GHz, while the grey pluses represent dimmer sources. The horizontal and vertical gray dashed lines are at $\alpha = -0.7$ (synchrotron sources). The diagonal gray dashed line corresponds to $\alpha_{1.4-20} = \alpha_{20-148}$.

The mean spectral index $\alpha_{20-148}^{\text{mean}}$ of the complete unbiased sample ($S > 70$ mJy) in the left panel of Fig. 20 is -0.36 ± 0.3 ($\sigma/\sqrt{N} = 0.04$). This is consistent with the findings of Marsden et al. (2014), who found that synchrotron-classified ACT-selected sources that were followed up with ATCA (Australia Telescope Compact Array) had a mean spectral index $\alpha_{20-148}^{\text{mean}} = -0.42^{+0.32}_{-0.26}$. This ACT sample was completely independent of the ACTPol D56 sample and indicates that the same radio source population is being

probed down to the low flux end. There are 5 sources with $\alpha_{20-148} > 0$: J000614-062337, J001736-051243, J020207-055902, J001752-023616, and J005735-012334. Of these, only J001736-051243 has a match in the Herschel SPIRE catalog. This source has also been identified as a DSFG in Gralla et al. (2018) defined by $\alpha_{1.4-148} > 1.0$.

The mean spectral index $\alpha_{1.4-148}^{\text{mean}}$ is -0.21 ± 0.25 ($\sigma/\sqrt{N} = 0.03$) when only considering sources brighter than 20 mJy at 148 GHz, and $\alpha_{1.4-148}^{\text{mean}}$ is -0.24 ± 0.26 ($\sigma/\sqrt{N} = 0.02$) when considering all cross-matched sources brighter than 10 mJy at 148 GHz.

In Fig. 21, we show a color-color comparison of 1.4–20 GHz versus 20–148 GHz spectral indices for the D56 sources detected above a flux threshold of 20 mJy and cross-identified with VLA-FIRST and AT20G catalogs. The incompleteness of the 20 GHz catalog does not only bias the 20–148 GHz spectral index distribution to steeper spectra, it also affects the 1.4–20 GHz spectral indices. If the 20 GHz catalog threshold were lower, one would see many more sources with steeper 1.4–20 GHz spectral index. The presence of many sources in the $\alpha_{1.4-20} > 0$, $\alpha_{20-148} < 0$ region is indicative of sources with a GHz peaked spectra not characterized by a single power law, as was also argued by de Zotti et al. (2010). It follows that the conventional classification of AGN-powered radio sources into flat and steep spectrum assuming a single power-law spectra is inaccurate at high radio frequencies. One of many factors (Tinti et al. 2005) that could lead to a more complex spectrum is a transition of the synchrotron emission from an optically thick self-absorbing regime characterized by a rising spectrum to an optically thin standard synchrotron regime characterized by a falling spectrum. These sources could have spectra peaking at frequencies of a few to tens of GHz.

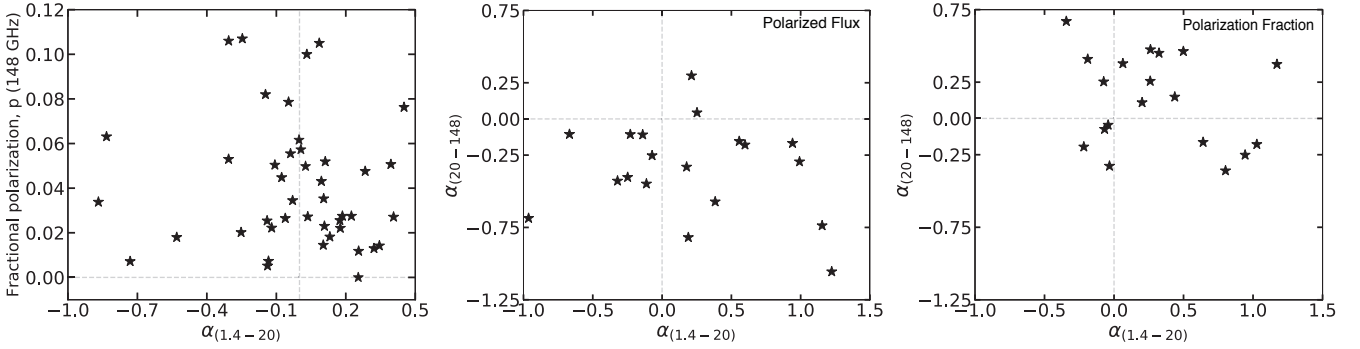


Figure 22. *Left:* Fractional polarization at 148 GHz plotted against 1.4–20 GHz spectral index for ACTPol-AT20G-NVSS cross-identified sources with total flux greater than 70 mJy (where the AT20G sample is complete) at 148 GHz. *Center and Right:* 1.4–20 GHz and 20–148 GHz spectral indices are shown for ACTPol-AT20G-NVSS cross-identified sources with measurements of polarized flux at all three frequencies. The center panel plots the indices derived from polarized flux P whereas the right panel plots the indices derived from fractional polarization p . There is no apparent correlation between the polarized flux spectral indices or the fractional polarization spectral indices in the color-color diagrams.

Based on the spectral index $\alpha_{1.4-20}$, we can classify the ACTPol-AT20G-VLAF cross-matched sources into steep ($\alpha_{1.4-20} < -0.5$) and flat ($\alpha_{1.4-20} > -0.5$) spectrum. The population probed here is predominantly comprised of flat spectrum sources, which is expected since sources with very steep spectra are unlikely to be above the detection threshold at a frequency as high as 148 GHz. Further, the AT20G sample is expected to be incomplete for $S_{20} < 70$ mJy. We expect that a complete unbiased sample will have almost equal numbers of steep and flat spectrum sources, as predicted by evolutionary models for radio sources in this flux density range (de Zotti et al. 2005). The mean spectral indices $\alpha_{1.4-148}^{\text{mean}}$ and $\alpha_{20-148}^{\text{mean}}$ are consistent with that of a source population dominated by synchrotron and free-free emitting AGN-powered radio sources comprised of Flat-Spectrum Radio Quasars (FSRQ) and BL Lacs. These are collectively referred to as blazars. Barthel (1989) argued that whether a source is a FSRQ or a BL Lac depends primarily on its axis of orientation relative to the observer. Powerful flat-spectrum radio quasars (FSRQs) are associated with a line-of-sight aligned with the AGN jet offering a view of the compact, Doppler-boosted, flat-spectrum base of the approaching jet (Urry & Padovani 1995). Low power radio sources are associated with BL Lac objects that have compact jet structures and are known to be variable and relatively highly polarized. They are characterized by flat radio spectra and a steep infrared spectra.

Fig. 22 shows color-color diagrams derived from measurements of polarized flux and fractional polarization. Only sources detected with total flux density greater than 74 mJy (1000 μ K) were included when making these plots. We do not find any correlation between the spectral indices derived from polarized intensity and polarization fraction. Neither is there any correlation between the spectral indices from total flux and polarized flux. Statistically, the polarized flux densities are on average much more similar between 1.4 and 148 GHz. Hence, the data favors a higher polarization fraction for radio sources at higher frequencies. This is consistent with the findings of Sajina et al. (2011) who report that sources on average are more polarized at higher frequencies.

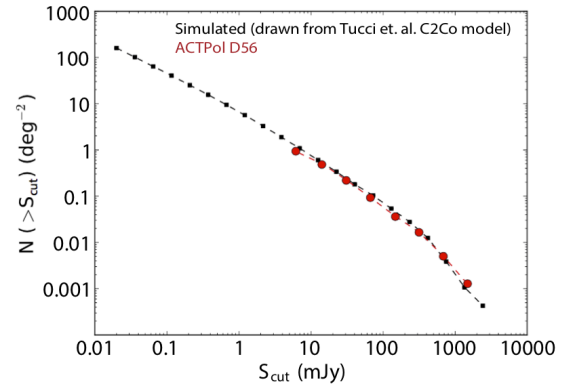


Figure 23. The number of synchrotron sources expected per square degree in a 148 GHz map above a given flux threshold, S_{cut} . Comparison between the number of ACTPol sources (red) and number of simulated sources (black) based on the C2Co model.

6 IMPACT OF POLARIZED SOURCES ON THE CMB EE MEASUREMENT

The dominant foreground contribution to the high- ℓ power spectrum at 148 GHz is from synchrotron (radio) and infrared (dusty) extragalactic sources, and the thermal and kinetic SZ effect from galaxy groups and clusters. The power from synchrotron sources is sensitive to the masking level at mm wavelengths being roughly proportional to the total flux threshold above which the sources are masked. This is because most of the power is contributed by the brightest few sources. However, the infrared population is not so sensitive to the masking level since most of the power comes from sources with low total flux at mm wavelengths. The source population we have analyzed here is mostly composed of synchrotron sources, and hence we can predict the synchrotron contribution to the Poisson spectrum for various levels of point source masking. Assuming that polarization angles of the extragalactic point sources are distributed randomly, they are expected to contribute equally on average to the Q and U Stokes parameters, and thus to E- and B-

Table 4. Predicted power from extragalactic synchrotron source population and crossover of its Poisson spectrum with the CMB EE spectrum for different levels of masking

S_{cut} (Jy)	$l_{\text{cross}}^{\text{PS EE}}$	$D_{l=5000}^{\text{PS EE}}$ (μK^2)
5	3100	4
1	3600	0.5
0.1	4600	0.04
0.01	5400	0.006
0.002	>6000	0.002

mode power spectra. For a Poisson-distributed population of such sources, the contribution to the polarization power spectrum in terms of the C_l is given by

$$C_{\ell, PS}^{EE} = C_{\ell, PS}^{BB} = \frac{1}{2} \left(\frac{dB}{dT} \right)^{-2} \int_0^{P_{\text{cut}}} \left(\frac{dN}{dP} \right) P^2 dP \quad (14)$$

where $dB/dT \approx 100e^x x^4 / (e^x - 1)^2 \mu\text{K}^{-1} \text{Jy sr}^{-1}$ is the multiplicative conversion factor to go from brightness temperature (in μK) to flux density (in Jy), $x = h\nu / (k_B T_{\text{CMB}})$, dN/dP is the differential source number counts per steradian with respect to polarized flux, P_{cut} is the masking threshold in terms of polarized flux, and the subscript “PS” refers to point sources. Since the polarized signal is weak, it is difficult to measure polarized source number counts. However, we can express $C_{\ell, PS}^{EE}$ in terms of the differential source number counts per steradian dN/dS with respect to total intensity and statistical estimates of the average fractional polarization of the source population squared $\langle p^2 \rangle$ as:

$$C_{\ell, PS}^{EE} = C_{\ell, PS}^{BB} = \frac{1}{2} \langle p^2 \rangle C_{\ell, PS}^{TT} \quad (15)$$

where, $C_{\ell, PS}^{TT} = \left(\frac{dB}{dT} \right)^{-2} \int_0^{S_{\text{cut}}} \left(\frac{dN}{dS} \right) S^2 dS$

The dN/dS we assume for predicting $C_{\ell, PS}^{EE}$ is based on the C2Co model which best fits the ACTPol source counts. The analytical calculation using equation (15) gives the upper and lower limits of the colored bands in Fig. 24 corresponding to $\langle p^2 \rangle = (0.028^2 + 0.054^2)$ and 0.028^2 , respectively for three different values of S_{cut} . In order to get a more accurate estimate of $C_{\ell, PS}^{EE}$, we use simulations. First, we estimate the expected number of sources per square degree above a given flux threshold S_{cut} , at 143 GHz directly from the C2Co dN/dS . This is consistent with the number of sources detected above a given S_{cut} in the D56 map as shown in the left panel of Fig. 23. Then, we simulate a $\sim 4600 \text{ deg}^2$ ($2^{13} \times 2^{13}$ pixels) source-only map by injecting sources drawn from the C2Co dN/dS model at random locations in the map. To simulate source-only Q and U maps, these sources are assigned fractional polarizations drawn from the best-fit model described in Section 4.4 which is a Gaussian distribution truncated at 0 with mean fractional polarization $p_m = 0.028$ and standard deviation $\sigma_{p_m} = 0.054$ (see left panel of Fig. 15), and polarization angles drawn from a flat distribution. The EE power spectrum computed from these maps gives the expected contribution of extragalactic synchrotron sources. Fig. 24 shows the residual $D_{\ell, PS}^{EE} = \ell(\ell+1)C_{\ell, PS}^{EE}/2\pi$ point source spectra for a few different levels of source masking based on total flux threshold S_{cut} , along with the CMB EE

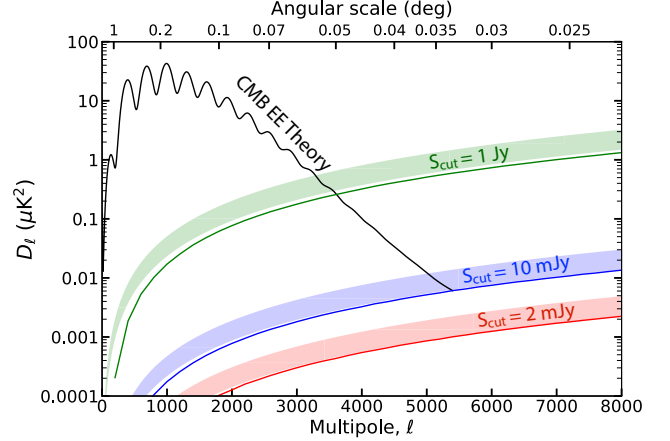


Figure 24. The expected power spectra of the extragalactic synchrotron source population alone (no noise is included in these simulations) with sources above some chosen total flux thresholds S_{cut} removed from the Stokes I , Q , and U maps. The colored lines correspond to a source population whose degree of fractional polarization is described by a truncated (at 0) Gaussian distribution with mean $p_m = 0.028$, standard deviation $\sigma_{p_m} = 0.054$ (as found in this work). The black curve shows the CMB theory EE power spectrum. The detection threshold of $S_{\text{cut}} = 2 \text{ mJy}$ is achievable by a future survey with a $1.4'$ beam and a $1 \mu\text{K-arcmin}$ noise level across 10% of the sky. The lower and upper limits of the colored bands correspond to analytical estimates using equation (15) and assuming $\langle p^2 \rangle = 0.028^2$ and $(0.028^2 + 0.054^2)$, respectively.

theory power spectrum. This shows that with appropriate point source masking in the Q and U maps, the crossing point between the EE spectrum from extragalactic sources and the measured CMB EE spectrum can be moved to higher ℓ 's. This represents the level of source subtraction expected to be required in order to measure the faint high- ℓ end of the EE spectrum.

Naess et al. (2014) had placed an upper limit on the contribution from sources $D_{l=3000}^{\text{PS EE}} < 2.4 \mu\text{K}^2$ based on ACTPol EE spectrum measurement with no sources masked. In Louis et al. (2017), sources above a total flux threshold $S_{\text{cut}} = 15 \text{ mJy}$ were masked in the total intensity map used for computing the ACTPol TT spectrum but no sources were masked in the Stokes Q and U maps used for computing the EE spectrum. Recent measurements of the EE spectrum reported by the SPTpol experiment in Henning et al. (2018) placed a 95% confidence upper limit on residual polarized Poisson power in the EE spectrum $D_{l=3000}^{\text{PS EE}} < 0.1 \mu\text{K}^2$ after masking all sources with total flux above 50 mJy. Based on our best fit model, we predict $D_{l=3000}^{\text{PS EE}} \sim 0.01 \mu\text{K}^2$ after applying a similar level of source masking. Though this prediction is based only on the contribution of synchrotron sources to the Poisson source spectrum, IR sources should not be significantly polarized compared to synchrotron sources (see Section 1). Table A4 shows our predictions for $D_{l=5000}^{\text{PS EE}}$ as well as expected values of ℓ at which the Poisson source spectra would cross the CMB theory EE spectrum for different levels of source masking. As we go to higher sensitivity maps, the source detection threshold goes down, and we can apply more aggressive source masks. In Fig. 24, the flux thresholds of 10 mJy and 2 mJy are representative of what

is achievable with ongoing and future CMB surveys (Abazajian et al. 2016), respectively. Assuming a $1.4'$ FWHM beam (similar to ACTPol) and an average map white noise level of $10 \mu\text{K-arcmin}$ and $1 \mu\text{K-arcmin}$ for a survey covering $\sim 10\%$ of the sky, the catalog completeness is expected to be near 100% at flux thresholds of 10 mJy and 2 mJy, respectively. Therefore, one could get a clean measurement of EE out to $\ell \approx 6000$ with a future survey.

7 SUMMARY

We have presented the polarization properties of extragalactic sources at 148 GHz from ACTPol observations during the 2013 and 2014 seasons covering 680 deg^2 of the sky in a region we refer to as “D56”. In our data, out of the 26 sources brighter than 215 mJy detected in total intensity, 14 ($\sim 60\%$) have a polarization signal with signal-to-noise ratio greater than 3 ($p > 3\sigma_p$). The average degree of polarization of these 26 sources, including the ones for which $p < 3\sigma_p$, is 2.6%. Using simulations, we find the distribution of the fractional polarization to be consistent with that of a polarized source population having mean fractional polarization $p_m = 0.028 \pm 0.005$ with $\sigma_{p_m} = 0.054$, and consistent with the scenario that the fractional polarization is independent of the total source intensity at least down to $S = 100 \text{ mJy}$. The measured level of average fractional polarization is consistent with typical numbers in the range 1–5% reported by other mm-wave and radio surveys. We compare the total and polarized flux measurements at 148 GHz with measurements at other frequencies from the VLA-FIRST, NVSS, AT20G, and Herschel SPIRE surveys and found that our source population is predominantly synchrotron with steepening, flat or peaked spectra. We did not find any evidence of correlation between the spectral indices derived from total flux and polarized flux. Our data favors higher levels of fractional polarization at higher frequencies for radio sources on average. The brightest source J000613–062336 in the D56 region, detected at 1.558° RA and -6.393° Dec, was three times brighter than the next brightest one. This is a previously known and widely studied highly variable BL Lac object by the name QSO B0003-066 at a redshift $z = 0.34$ (D’Abrusco et al. 2014). It has also been seen in the optical. We also present predictions for the contribution of power from extragalactic sources to the CMB EE spectrum and predict the level of source masking that would be required to enable precision measurements of the faint high- ℓ end of the EE spectrum. The lack of foregrounds in EE compared to TT is promising for constraining cosmology with high resolution measurements of the E-mode polarization. With future surveys, it could be possible to measure the EE spectrum out to $\ell \approx 6000$. Looking ahead, multi-frequency data from the subsequent seasons of ACTPol and AdvACT observations in five frequency bands spanning 25 to 280 GHz will constrain the spectral signature of thousands of point sources over a large frequency range to unambiguously distinguish between radio and dusty sources and help find new, previously unidentified sources. It will also significantly improve the statistics on the measurements of the fractional polarization of extragalactic sources at millimeter wavelengths and potentially detect hundreds of sources in polarization.

ACKNOWLEDGEMENTS

This work was supported by the U.S. National Science Foundation through awards AST-1440226, AST-0965625 and AST- 0408698 for the ACT project, as well as awards PHY-1214379 and PHY-0855887. ACT operates in the Parque Astronómico Atacama in northern Chile under the auspices of the Comisión Nacional de Investigación Científica y Tecnológica de Chile (CONICYT). R. Datta’s research was supported by an appointment to the NASA Postdoctoral Program at the NASA Goddard Space Flight Center, administered by Universities Space Research Association under contract with NASA. R. Datta would also like to acknowledge support from the Balzan foundation in the form of a Center for Cosmological Studies (CCS) Fellowship at the Johns Hopkins University and the Rackham Predoctoral Fellowship awarded by the University of Michigan during the initial phase of this work. CL thanks CONICYT for grant Anillo ACT-1417. LM is funded by CONICYT FONDECYT grant 3170846. R. Dunner acknowledges CONICYT for grants FONDECYT 1141113, Anillo ACT-1417, QUIMAL 160009 and BASAL PFB-06 CATA. M. Hilton acknowledges financial support from the National Research Foundation, the South African Square Kilometre Array project, and the University of KwaZulu-Natal.

REFERENCES

- Abazajian K. N., et al., 2016, preprint, ([arXiv:1610.02743](https://arxiv.org/abs/1610.02743))
- Abitbol M. H., et al., 2017, preprint, ([arXiv:1706.02464](https://arxiv.org/abs/1706.02464))
- Agudo I., Thum C., Wiesemeyer H., Krichbaum T. P., 2010, The Astrophysical Journal Supplement Series, 189, 1
- Angel J. R. P., Stockman H. S., 1980, *ARA&A*, 18, 321
- Barthel P., 1989, *Scientific American*, 260, 20
- Battye R. A., Browne I. W. A., Peel M. W., Jackson N. J., Dickinson C., 2011, *MNRAS*, 413, 132
- Becker R. H., White R. L., Helfand D. J., 1995, *ApJ*, 450, 559
- Benson B. A., et al., 2014, in Millimeter, Submillimeter, and Far-Infrared Detectors and Instrumentation for Astronomy VII. p. 91531P ([arXiv:1407.2973](https://arxiv.org/abs/1407.2973)), doi:10.1117/12.2057305
- Bonavera L., Gonzalez-Nuevo J., De Marco B., Argüeso F., Toffolatti L., 2017a, preprint, ([arXiv:1705.10603](https://arxiv.org/abs/1705.10603))
- Bonavera L., González-Nuevo J., Argüeso F., Toffolatti L., 2017b, *MNRAS*, 469, 2401
- CCAT-prime 2017, <http://www.ccatobservatory.org>
- Calabrese E., et al., 2014, *J. Cosmology Astropart. Phys.*, 8, 010
- Casey C. M., Narayanan D., Cooray A., 2014, *Phys. Rep.*, 541, 45
- Condon J. J., Cotton W. D., Greisen E. W., Yin Q. F., Perley R. A., Taylor G. B., Broderick J. J., 1998, *AJ*, 115, 1693
- Crawford T. M., Switzer E. R., Holzapfel W. L., Reichardt C. L., Marrone D. P., Vieira J. D., 2010, *ApJ*, 718, 513
- D’Abrusco R., Massaro F., Paggi A., Smith H. A., Masetti N., Landoni M., Tosti G., 2014, *ApJS*, 215, 14
- Dünner R., et al., 2013, *ApJ*, 762, 10
- Galli S., et al., 2014, *Phys. Rev. D*, 90, 063504
- Galluzzi V., Massardi M., 2016, *International Journal of Modern Physics D*, 25, 1640005
- Geach J. E., et al., 2015, *MNRAS*, 452, 502
- Gralla M. B., Marriage T., ACTPol C., 2018, In preparation
- Grant J. K., Taylor A. R., Stil J. M., Landecker T. L., Kothes R., Ransom R. R., Scott D., 2010, *ApJ*, 714, 1689
- Graves J. S., Holland W. S., 2002, in Cecchini S., Cortiglioni S., Sault R., Sbarra C., eds, American Institute of Physics Con-

ference Series Vol. 609, Astrophysical Polarized Backgrounds, pp 267–270, [doi:10.1063/1.1471859](https://doi.org/10.1063/1.1471859)

Hales C. A., Norris R. P., Gaensler B. M., Middelberg E., 2014, *MNRAS*, **440**, 3113

Hasselfield M., et al., 2013, *ApJS*, **209**, 17

Helou G., Soifer B. T., Rowan-Robinson M., 1985, *ApJ*, **298**, L7

Henderson S. W., et al., 2016, *Journal of Low Temperature Physics*, **184**, 772

Henning J. W., et al., 2018, *ApJ*, **852**, 97

Huffenberger K. M., et al., 2015, *ApJ*, **806**, 112

Klein U., Mack K.-H., Gregorini L., Vigotti M., 2003, *A&A*, **406**, 579

López-Caniego M., Massardi M., González-Nuevo J., Lanz L., Herranz D., De Zotti G., Sanz J. L., Argüeso F., 2009, *ApJ*, **705**, 868

López-Caraballo C. H., Rubiño-Martín J. A., Rebolo R., Génova-Santos R., 2011, *ApJ*, **729**, 25

Louis T., et al., 2017, *J. Cosmology Astropart. Phys.*, **6**, 031

Maier D., Tenzer C., Santangelo A., 2014, *PASP*, **126**, 459

Marriage T. A., et al., 2011, *ApJ*, **731**, 100

Marsden D., et al., 2014, *MNRAS*, **439**, 1556

Massardi M., Galluzzi V., Paladino R., Burigana C., 2016, *International Journal of Modern Physics D*, **25**, 1640009

Matthews B. C., McPhee C. A., Fissel L. M., Curran R. L., 2009, *ApJS*, **182**, 143

Mesa D., Baccigalupi C., De Zotti G., Gregorini L., Mack K.-H., Vigotti M., Klein U., 2002, *A&A*, **396**, 463

Mocanu L. M., et al., 2013, *ApJ*, **779**, 61

Montier L., Plaszczynski S., Levrier F., Tristram M., Alina D., Ristorcelli I., Bernard J.-P., 2015a, *A&A*, **574**, A135

Montier L., Plaszczynski S., Levrier F., Tristram M., Alina D., Ristorcelli I., Bernard J.-P., Guillet V., 2015b, *A&A*, **574**, A136

Murphy T., et al., 2010, *MNRAS*, **402**, 2403

Naess S., et al., 2014, *J. Cosmology Astropart. Phys.*, **10**, 007

Nartallo R., Gear W. K., Murray A. G., Robson E. I., Hough J. H., 1998, *MNRAS*, **297**, 667

Page L., et al., 2003, *The Astrophysical Journal*, **585**, 566

Planck Collaboration et al., 2011, *A&A*, **536**, A7

Planck Collaboration et al., 2013, *A&A*, **550**, A133

Planck Collaboration et al., 2016, *A&A*, **594**, A26

Plaszczynski S., Montier L., Levrier F., Tristram M., 2014, *MNRAS*, **439**, 4048

Puglisi G., et al., 2017, preprint, ([arXiv:1712.09639](https://arxiv.org/abs/1712.09639))

Quinn J. L., 2012, *A&A*, **538**, A65

Ricci R., Prandoni I., Gruppioni C., Sault R. J., De Zotti G., 2004, *A&A*, **415**, 549

Rubiño-Martín J. A., López-Caraballo C. H., Génova-Santos R., Rebolo R., 2012, *Advances in Astronomy*, **2012**, 351836

SO 2017, www.simonsobservatory.org

Sadler E. M., et al., 2006, *MNRAS*, **371**, 898

Saikia D. J., Salter C. J., 1988, *Ann. Rev. Astron. Astrophys.*, **26**, 93

Sajina A., Partridge B., Evans T., Steff S., Vechik N., Myers S., Dicker S., Korngut P., 2011, *ApJ*, **732**, 45

Schulz B. e. a., 2017, <http://archives.esac.esa.int/>

Seiffert M., Borys C., Scott D., Halpern M., 2007, *MNRAS*, **374**, 409

Seljak U., Hirata C. M., 2004, *Phys. Rev. D*, **69**, 043005

Serkowski K., 1958, *Acta Astron.*, **8**, 135

Simmons J. F. L., Stewart B. G., 1985, *A&A*, **142**, 100

Stil J. M., Keller B. W., George S. J., Taylor A. R., 2014, *The Astrophysical Journal*, **787**, 99

Subrahmanyan R., Ekers R. D., Saripalli L., Sadler E. M., 2010, *MNRAS*, **402**, 2792

Taylor A. R., et al., 2007, *ApJ*, **666**, 201

Thornton R. J., et al., 2016, *ApJS*, **227**, 21

Tinti S., Dallacasa D., de Zotti G., Celotti A., Stanghellini C., 2005, *A&A*, **432**, 31

Toffolatti L., Argüeso Gomez F., de Zotti G., Mazzei P., Franceschini A., Danese L., Burigana C., 1998, *MNRAS*, **297**, 117

Trombetti T., Burigana C., De Zotti G., Galluzzi V., Massardi M., 2018, *A&A*, **618**, A29

Tucci M., Toffolatti L., 2012, *Advances in Astronomy*, **2012**, 624987

Tucci M., Martínez-González E., Toffolatti L., González-Nuevo J., De Zotti G., 2004, *MNRAS*, **349**, 1267

Urry C. M., Padovani P., 1995, *PASP*, **107**, 803

Vieira J. D., et al., 2010, *ApJ*, **719**, 763

Vieira J. D., et al., 2013, *Nature*, **495**, 344

Wardle J. F. C., Kronberg P. P., 1974, *ApJ*, **194**, 249

de Zotti G., Ricci R., Mesa D., Silva L., Mazzotta P., Toffolatti L., González-Nuevo J., 2005, *A&A*, **431**, 893

de Zotti G., Massardi M., Negrello M., Wall J., 2010, *A&ARv*, **18**, 1

APPENDIX A: FLUXES AND EFFECTIVE FREQUENCIES OF COMPACT SOURCES

Compact extragalactic sources appear in our maps as unresolved hot spots with the profile of the beam. In this appendix, we show how we convert the measured source amplitudes in CMB temperature units to flux densities in Jansky (Jy). A source's emission as a function of frequency is parametrized as $S_\nu \propto (\nu/\nu_e)^\alpha$ where α denotes the source spectral index and ν_e is a reference frequency. The instrument's frequency response is characterized with a passband, $f(\nu)$, and an antenna gain that also depends on frequency. We parametrize the latter as:

$$G_m(\nu) = \frac{4\pi}{\Omega_B} \left(\frac{\nu}{\nu_{RJ}} \right)^{-2\beta} \quad (\text{A1})$$

The quantity β scales the size of the FWHM and is generally between 0 and -1 . Because β is negative, at higher frequencies the beam is narrower and the gain is higher. For ACT, β is near -1 . The gain is scaled to the value measured with planets which are well approximated as Rayleigh-Jeans sources ($\alpha = 2$).

Following Page et al. (2003) we define an effective frequency

$$\nu_e = \frac{\int \nu f(\nu) \nu^{-2(1+\beta)+\alpha} d\nu}{\int f(\nu) \nu^{-2(1+\beta)+\alpha} d\nu} \quad (\text{A2})$$

and CMB temperature to flux conversion factor

$$\Gamma = \frac{c^2}{2k_B \Omega_B \nu_e^\alpha \nu_{RJ}^{-2\beta}} \frac{\int \nu^{-2(1+\beta)+\alpha} f(\nu) d\nu}{\int f(\nu) d\nu} 10^{-20} [\mu\text{K}/\text{Jy}] \quad (\text{A3})$$

Let us say the source has a temperature spectrum of $T_{\text{src}} \propto \nu^{\alpha-2}$. We convert the measured source amplitude in CMB temperature units to a flux density at its effective central frequency as follows:

(i) Convert to a brightness temperature for the source by dividing by the factor:

$$\frac{\delta T_{\text{CMB}}}{\delta T_{\text{src}}} = \frac{\delta S_{\nu, \text{src}}}{\delta T_{\text{src}}} \left(\frac{\delta S_{\nu, \text{CMB}}}{\delta T_{\text{CMB}}} \right)^{-1} = \left(\frac{\nu}{\nu_e} \right)^{\alpha-2} \frac{(e^x - 1)^2}{x^2 e^x} \quad (\text{A4})$$

with $x = \frac{h\nu_e}{k_B T_{\text{CMB}}}$

Note that this is simply $\delta T_{\text{CMB}}/\delta T_{\text{RJ}}$ if $\alpha = 2$ and $\nu_e = \nu_{\text{RJ}}$.

(ii) Find the flux by dividing the temperature from step (i) by Γ as computed above.

(iii) To find the source flux at a different frequency than its effective central frequency, we can use the scaling relations $S_\nu \propto (\nu/\nu_e)^\alpha$ or $T_\nu \propto (\nu/\nu_e)^{\alpha-2}$. Note that this assumes the source has a simple power law spectrum.

Tables A1 and A2 give the conversion factors $\delta T_{\text{CMB}}/\delta T_{\text{RJ}}$ and Γ for $\beta = 0$ and -1.0 for different types of sources. The uncertainties in the conversion factors include uncertainties in the measurements of the central frequency and the beam solid angle. These tables update the numbers in Table 1 of Thornton et al. (2016). Since most of the sources in this work are synchrotron dominated, the measured source fluxes in Table A4 are reported at $\nu_e = 147.6$ GHz, which is the central frequency to synchrotron sources ($\alpha = -0.7$) assuming $\beta = -1$. If any of these sources has a known spectral index that is different from -0.7 , a multiplicative color correction factor can be used to get its true flux at 147.6 GHz. We provide these factors along with uncertainties for a range of values of α from -2.0 to $+4.0$ in steps of 0.2 in Table A3. Note that the flux density uncertainties quoted in Table A4 do not include errors in the measurement of the central frequency or the beam solid angle. The complete uncertainty should be obtained by combining the errors in Tables A2 and A4 in quadrature.

Below is a description of the columns in Table A4:

1. ID: Source ID in the format “ACTPol-D56 J[hh mm ss][deg min sec]” (* indicates extended source)
2. RA: J2000 right ascension of the source in decimal degrees
3. dec: J2000 declination of the source in decimal degrees
4. S/N: Signal-to-noise ratio of the detection in total intensity
5. T_{CMB} : Source amplitude in CMB temperature units (μK) along with the 1σ uncertainty
6. Stokes Q : Stokes Q amplitude in CMB temperature units (μK) for sources brighter than 30 mJy in total flux density along with the 1σ uncertainty
7. Stokes U : Stokes U amplitude in CMB temperature units (μK , following the IAU standard) for sources brighter than 30 mJy in total flux density along with the 1σ uncertainty
8. S_{raw} : Raw measured flux density in mJy units at 147.6 GHz (assumes a source spectral index of -0.7) along with the 1σ uncertainty
9. S_{deb} : Deboosted flux density in mJy units (only sources dimmer than 100 mJy are deboosted) along with the negative and positive 1σ uncertainties
10. S/N_p : Signal-to-noise ratio in polarization
11. p_{WK} : Percentage fractional polarization estimated using the Wardle-Kronberg estimator along with the negative and positive 1σ uncertainties
12. p_x : Percentage fractional polarization estimated using the 2-way data splits along with the negative and positive 1σ uncertainties
13. pol ang: Polarization angle of the source following the IAU standard (only for sources detected in polarization at a significance larger than 3-sigma) along with the 1σ uncertainty
14. var?: for sources observed during both seasons, check-

mark indicates that the variation in the measured source flux density between the 2013 (S13) and 2014 (S14) observing seasons is greater than 40%

15. V?: checkmark indicates that the source has a cross-match in the VLA FIRST 1.4 GHz catalog

16. A?: checkmark indicates that the source has a cross-match in the AT20G 20 GHz catalog

17. S?: checkmark indicates that the source has a cross-match in the Herschel SPIRE 600 GHz catalog

Table A1. Central frequencies for compact sources (except CMB) and conversion factors to go from a measured source amplitude in temperature units to flux density assuming $\beta = 0$ and solid angle of the beam used in the matched filtering $\Omega_B = 182 \pm 3$ nsr

Source	Sync, $S_\nu \propto \nu^{-0.7}$	FF, $S_\nu \propto \nu^{-0.1}$	CMB	RJ, $S_\nu \propto \nu^2$	Dust, $S_\nu \propto \nu^{3.7}$
ν_e (GHz)	144.9 \pm 2.4	145.7 \pm 2.4	148.6 \pm 2.4	148.6 \pm 2.4	150.8 \pm 2.4
$\frac{\delta T_{CMB}}{\delta T_{RJ}}$	1.67 \pm 0.03	1.68 \pm 0.03	1.71 \pm 0.03	1.71 \pm 0.03	1.74 \pm 0.03
Γ (μ K/Jy)	8337 \pm 169	8331 \pm 138		8109 \pm 294	7725 \pm 477

Table A2. Central frequencies for compact sources (except CMB) and conversion factors to go from a measured source amplitude in temperature units to flux density assuming $\beta = -1$ and solid angle of the beam used in the matched filtering $\Omega_B = 182 \pm 3$ nsr

Source	Sync, $S_\nu \propto \nu^{-0.7}$	FF, $S_\nu \propto \nu^{-0.1}$	CMB	RJ, $S_\nu \propto \nu^2$	Dust, $S_\nu \propto \nu^{3.7}$
ν_e (GHz)	147.6 \pm 2.4	148.4 \pm 2.4	151.2 \pm 2.4	151.2 \pm 2.4	153.3 \pm 2.4
$\frac{\delta T_{CMB}}{\delta T_{RJ}}$	1.70 \pm 0.03	1.71 \pm 0.03	1.75 \pm 0.03	1.75 \pm 0.03	1.772 \pm 0.03
Γ (μ K/Jy)	7833 \pm 296	7829 \pm 282		7634 \pm 502	7289 \pm 501

Table A3. Color corrections: multiplicative factors $C(\alpha)$ for computing source flux densities at 147.6 GHz for a given source spectral index α and starting with the measured flux densities reported in Table A4

Source Spectral Index α	$C(\alpha, \beta = 0)$	$C(\alpha, \beta = -1)$	Source Spectral Index α	$C(\alpha, \beta = 0)$	$C(\alpha, \beta = -1)$
-2.0	0.92 \pm 0.03	1.00 \pm 0.03	+1.2	0.95 \pm 0.04	0.98 \pm 0.03
-1.8	0.93 \pm 0.03	1.00 \pm 0.03	+1.4	0.95 \pm 0.04	0.97 \pm 0.03
-1.6	0.93 \pm 0.04	1.00 \pm 0.03	+1.6	0.95 \pm 0.04	0.97 \pm 0.03
-1.4	0.93 \pm 0.04	1.00 \pm 0.03	+1.8	0.95 \pm 0.04	0.96 \pm 0.03
-1.2	0.94 \pm 0.04	1.00 \pm 0.03	+2.0	0.95 \pm 0.04	0.96 \pm 0.03
-1.0	0.94 \pm 0.04	1.00 \pm 0.03	+2.2	0.95 \pm 0.04	0.95 \pm 0.03
-0.8	0.94 \pm 0.04	1.00 \pm 0.03	+2.4	0.94 \pm 0.04	0.94 \pm 0.03
-0.6	0.95 \pm 0.04	1.00 \pm 0.03	+2.6	0.94 \pm 0.04	0.94 \pm 0.03
-0.4	0.95 \pm 0.04	1.00 \pm 0.03	+2.8	0.94 \pm 0.04	0.93 \pm 0.03
-0.2	0.95 \pm 0.04	1.00 \pm 0.03	+3.0	0.93 \pm 0.04	0.93 \pm 0.03
0.0	0.95 \pm 0.04	1.00 \pm 0.03	+3.2	0.93 \pm 0.04	0.92 \pm 0.03
+0.2	0.95 \pm 0.04	0.99 \pm 0.03	+3.4	0.93 \pm 0.03	0.91 \pm 0.03
+0.4	0.95 \pm 0.04	0.99 \pm 0.03	+3.6	0.92 \pm 0.03	0.90 \pm 0.03
+0.6	0.95 \pm 0.04	0.99 \pm 0.03	+3.8	0.92 \pm 0.03	0.90 \pm 0.03
+0.8	0.95 \pm 0.04	0.98 \pm 0.03	+4.0	0.91 \pm 0.03	0.89 \pm 0.03
+1.0	0.95 \pm 0.04	0.98 \pm 0.03			

Table A4: Catalog of point sources from the ACTPol D56 survey at 148 GHz with total flux density S_{148} greater than 30 mJy. The full catalog is available on LAMBDA. The flux densities reported here are at 147.6 GHz, and assume a source spectral index of -0.7 .

ID ACTPol-D56	RA (deg)	dec (deg)	S/N	T _{CMB} (μ K)	Stokes Q (μ K)	Stokes U (μ K)	S _{raw} (mJy)	S _{deb} (mJy)	S/N _p	PWK (%)	P \times (%)	pol ang (deg)	var?	V?	A?	S?
J000111-002015	0.2969	-0.3375	21.0	616 \pm 29	46.3 \pm 2.1	47.3 $^{+7.7}_{-7.7}$	✓
J000118-074627	0.3250	-7.7744	60.9	1938 \pm 32	38 \pm 33	68 \pm 33	145.6 \pm 2.3	..	2.4	3.7 $^{+1.7}_{-0.9}$	2.7 $^{+2.4}_{-2.4}$..	✓	✓
J000257-002445	0.7391	-0.4125	13.9	403 \pm 29	30.3 \pm 2.1	29.3 $^{+5.6}_{-5.6}$	✓	✓
J000613-062336*	1.5578	-6.3935	1238	43452 \pm 35	2060 \pm 36	1438 \pm 36	3261.4 \pm 2.6	..	68.7	5.8 $^{+0.2}_{-0.2}$	5.7 $^{+0.1}_{-0.1}$	+17 \pm 1	..	✓	✓	..
J000622-000422	1.5943	-0.0729	37.6	1046 \pm 28	-54 \pm 33	-88 \pm 33	78.5 \pm 2.1	77.6 $^{+13.8}_{-12.8}$	3.1	9.4 $^{+3.0}_{-2.9}$	6.3 $^{+4.5}_{-4.5}$	-61 \pm 10	..	✓	✓	..
J001000-043347	2.5016	-4.5632	78.2	2490 \pm 32	-45 \pm 33	93 \pm 33	186.9 \pm 2.4	..	3.1	4.0 $^{+1.3}_{-1.3}$	2.8 $^{+1.9}_{-1.9}$	+58 \pm 10	..	✓	✓	..
J001130+005756	2.8771	+0.9657	46.8	1230 \pm 26	-71 \pm 31	2 \pm 31	92.3 \pm 2.0	93.2 $^{+15.7}_{-15.5}$	2.3	5.3 $^{+2.6}_{-1.3}$	3.7 $^{+3.6}_{-1.9}$	✓
J001354-042351	3.4755	-4.3976	87.9	2873 \pm 33	49 \pm 34	-62 \pm 34	215.7 \pm 2.5	..	2.3	2.5 $^{+1.2}_{-0.6}$	2.8 $^{+1.7}_{-1.7}$	✓	✓	..
J001611-001509	4.0458	-0.2526	72.5	2309 \pm 32	-7 \pm 33	65 \pm 33	173.3 \pm 2.4	..	2.0	2.5 $^{+1.5}_{-0.7}$	1.8 $^{+2.0}_{-1.8}$	✓	✓	..
J001709-065036	4.2896	-6.8433	19.3	580 \pm 30	43.6 \pm 2.3	45.5 $^{+7.1}_{-10.5}$	✓	✓	..
J001735-051242*	4.3990	-5.2119	140.7	4670 \pm 33	106 \pm 34	199 \pm 34	350.5 \pm 2.5	..	6.5	4.8 $^{+0.7}_{-0.8}$	5.0 $^{+1.0}_{-1.0}$	+31 \pm 5	..	✓	✓	✓
J001752-023616	4.4677	-2.6045	41.6	1160 \pm 28	6 \pm 33	119 \pm 33	87.0 \pm 2.1	85.5 $^{+14.3}_{-13.9}$	3.6	10.0 $^{+2.6}_{-2.7}$	10.0 $^{+4.1}_{-4.1}$	+44 \pm 8	..	✓	✓	..
J001834-062838	4.6422	-6.4773	15.4	474 \pm 31	35.6 \pm 2.3	34.3 $^{+6.3}_{-7.6}$	✓	✓	..
J001917-010356	4.8229	-1.0657	23.3	651 \pm 28	48.8 \pm 2.1	48.6 $^{+8.4}_{-8.0}$	✓	✓	..
J002238+014704	5.6594	+1.7847	41.7	1069 \pm 26	80.2 \pm 1.9	78.2 $^{+13.9}_{-12.9}$..	0.0 $^{+0.4}_{-0.0}$	0.0 $^{+4.1}_{-0.0}$	✓
J002400-081114	6.0037	-8.1872	93.2	3148 \pm 34	25 \pm 35	15 \pm 35	236.3 \pm 2.5	0.0 $^{+1.3}_{-0.0}$	0.0 $^{+1.6}_{-0.0}$	✓	✓	..
J002446-041204	6.1917	-4.2012	24.2	687 \pm 28	51.6 \pm 2.1	51.7 $^{+9.1}_{-8.6}$	✓	✓	..
J002733+045915	6.8885	+4.9876	25.5	681 \pm 27	51.1 \pm 2.0	50.8 $^{+8.4}_{-8.4}$	✓
J002901-011339	7.2542	-1.2277	47.5	1320 \pm 28	16 \pm 33	28 \pm 33	99.1 \pm 2.1	98.4 $^{+16.6}_{-15.8}$..	0.0 $^{+3.2}_{-0.0}$	2.2 $^{+0.0}_{-2.2}$	✓	✓	..
J003007-000015	7.5328	-0.0042	15.0	418 \pm 28	31.4 \pm 2.1	30.3 $^{+6.1}_{-6.0}$	✓	✓	..
J003031-021154	7.6323	-2.1985	94.4	3024 \pm 32	-38 \pm 33	12 \pm 33	227.0 \pm 2.4	..	1.2	0.9 $^{+1.1}_{-0.6}$	1.2 $^{+1.6}_{-1.2}$	✓	✓	✓
J003259+051010	8.2474	+5.1695	18.3	509 \pm 28	38.2 \pm 2.1	37.7 $^{+7.3}_{-8.3}$	✓
J003307-042933	8.2802	-4.4926	15.6	457 \pm 29	34.3 \pm 2.2	33.7 $^{+5.9}_{-7.3}$	✓	✓	..
J003443-005411	8.6828	-0.9032	35.4	1003 \pm 28	-16 \pm 34	41 \pm 34	75.3 \pm 2.1	73.9 $^{+12.4}_{-12.1}$	1.3	..	3.5 $^{+4.8}_{-3.5}$	✓	✓	..
J003546-083552	8.9427	-8.5979	57.2	2103 \pm 37	61 \pm 44	-146 \pm 44	157.9 \pm 2.8	..	3.6	7.3 $^{+1.9}_{-2.0}$	7.6 $^{+3.0}_{-3.0}$	-34 \pm 8	..	✓	✓	..
J003635-031812	9.1474	-3.3034	15.8	437 \pm 28	32.8 \pm 2.1	32.4 $^{+5.9}_{-6.2}$	✓	✓	..
J003637-024007	9.1568	-2.6692	14.8	406 \pm 27	30.5 \pm 2.0	29.5 $^{+5.6}_{-5.6}$	✓	✓	..
J003704-010905	9.2667	-1.1516	48.3	1375 \pm 28	-5 \pm 34	42 \pm 34	103.2 \pm 2.1	..	1.3	2.4 $^{+2.4}_{-1.3}$	3.4 $^{+3.5}_{-3.4}$	✓	✓	..
J003816-012204	9.5688	-1.3678	27.8	774 \pm 28	58.1 \pm 2.1	59.5 $^{+9.6}_{-9.6}$	✓	✓	..
J003820-020741	9.5854	-2.1281	133.7	4369 \pm 33	-24 \pm 34	3 \pm 34	327.9 \pm 2.5	0.0 $^{+0.8}_{-0.0}$	0.7 $^{+0.0}_{-0.7}$	✓	✓	✓
J003849-011719	9.7057	-1.2887	21.2	593 \pm 28	44.5 \pm 2.1	46.0 $^{+7.4}_{-10.5}$	✓	✓	..
J003852-012156	9.7182	-1.3658	20.5	571 \pm 28	42.8 \pm 2.1	44.9 $^{+7.2}_{-10.4}$	✓	✓	..
J003913-025708	9.8057	-2.9524	30.0	821 \pm 27	61.6 \pm 2.1	61.9 $^{+9.8}_{-9.8}$	✓	✓	..
J003919+031955	9.8292	+3.3321	21.1	630 \pm 30	47.3 \pm 2.2	47.3 $^{+7.9}_{-7.8}$	✓
J004013+012549	10.0563	+1.4304	72.3	2164 \pm 30	-32 \pm 31	97 \pm 31	162.4 \pm 2.2	..	3.3	4.5 $^{+1.4}_{-1.4}$	4.7 $^{+2.0}_{-2.0}$	+54 \pm 9	..	✓	..	✓
J004020-004031*	10.0839	-0.6755	29.5	847 \pm 29	63.5 \pm 2.2	63.0 $^{+10.8}_{-10.4}$	✓	✓	..
J004057-014632	10.2401	-1.7758	102.5	3295 \pm 32	-145 \pm 33	-5 \pm 33	247.3 \pm 2.4	..	4.3	4.3 $^{+0.9}_{-1.0}$	4.5 $^{+1.4}_{-1.4}$	-79 \pm 4	..	✓	✓	✓
J004300-075354	10.7500	-7.8984	21.2	663 \pm 31	49.8 \pm 2.3	49.7 $^{+8.5}_{-8.2}$	✓	✓	..
J004332+002452	10.8870	+0.4146	17.5	476 \pm 27	35.7 \pm 2.0	34.3 $^{+6.3}_{-7.7}$	✓
J004345-025108	10.9406	-2.8522	20.2	533 \pm 26	40.0 \pm 2.0	40.7 $^{+7.1}_{-9.2}$	✓	✓	..
J004346+050259	10.9438	+5.0498	24.1	643 \pm 27	48.3 \pm 2.0	48.2 $^{+8.2}_{-7.9}$	✓	..	✓
J004404+010152	11.0188	+1.0313	24.8	661 \pm 27	49.6 \pm 2.0	49.6 $^{+8.5}_{-8.2}$	✓
J004705+031959	11.7745	+3.3331	60.9	1665 \pm 27	27 \pm 32	18 \pm 32	125.0 \pm 2.1	0.4 $^{+2.3}_{-0.4}$	0.0 $^{+0.0}_{-0.0}$	✓
J004943+023705	12.4302	+2.6181	46.3	1133 \pm 24	-60 \pm 29	22 \pm 29	85.0 \pm 1.8	82.9 $^{+14.7}_{-13.9}$	2.2	5.1 $^{+2.6}_{-1.3}$	4.6 $^{+3.7}_{-3.7}$	✓	..	✓
J005021-045223	12.5896	-4.8731	114.8	3733 \pm 33	-3 \pm 34	-100 \pm 34	280.2 \pm 2.4	..	2.9	2.5 $^{+0.9}_{-0.9}$	2.7 $^{+1.3}_{-1.3}$	✓	✓	..
J005108-065003	12.7844	-6.8344	165.9	5837 \pm 35	47 \pm 36	-101 \pm 36	438.1 \pm 2.6	..	3.1	1.8 $^{+0.6}_{-0.6}$	1.8 $^{+0.9}_{-0.9}$	-33 \pm 10	..	✓	✓	..
J005159+042742	12.9964	+4.4618	24.5	737 \pm 30	55.3 \pm 2.3	56.6 $^{+9.6}_{-9.6}$	✓
J005205+003537	13.0240	+0.5938	23.1	620 \pm 27	46.5 \pm 2.0	47.3 $^{+7.9}_{-7.7}$	✓
J005717-002435	14.3208	-0.4099	23.3	641 \pm 28	48.1 \pm 2.1	48.1 $^{+8.2}_{-8.0}$	✓	✓	..
J005734-012334*	14.3953	-1.3929	47.7	1315 \pm 28	71 \pm 33	19 \pm 33	98.7 \pm 2.1	98.4 $^{+16.5}_{-15.7}$	2.2	5.1 $^{+2.5}_{-1.3}$	5.6 $^{+3.5}_{-3.5}$	✓
J005805-053953	14.5208	-5.6650	106.8	3342 \pm 31	134 \pm 32	92 \pm 32	250.9 \pm 2.3	..	5.0	4.8 $^{+0.7}_{-1.0}$	4.8 $^{+1.3}_{-1.4}$	+17 \pm 6	..	✓	✓	..
J005826+032911	14.6099	+3.4865	19.0	562 \pm 30	42.2 \pm 2.2	43.3 $^{+7.2}_{-9.9}$	✓
J005905+000652	14.7729	+0.1146	106.5	3355 \pm 32	-32 \pm 32	94 \pm 32	251.8 \pm 2.4	..	3.1	2.8 $^{+0.9}_{-0.9}$	2.7 $^{+1.4}_{-1.4}$	+54 \pm 10	..	✓	..	✓
J010230-080432	15.6271	-8.0757	22.4	620 \pm 28	46.5 \pm 2.1	47.3 $^{+7.7}_{-7.7}$	✓
J010237+042107	15.6547	+4.3521	16.7	488 \pm 29	36.6 \pm 2.2	35.9 $^{+6.8}_{-7.8}$	✓
J010622-015536	16.5953	-1.9269	19.5	538 \pm 28	40.4 \pm 2.1	41.1 $^{+7.2}_{-9.4}$	✓	✓	..
J010643-031536	16.6797	-3.2601	60.6	1583 \pm 26	-36 \pm 31	78 \pm 31	118.8 \pm 2.0	..	2.8	5.1 $^{+2.0}_{-1.0}$	5.3 $^{+2.8}_{-2.8}$	✓	..	✓
J010728+033351	16.8693	+3.5643	36.9	1096 \pm 30	-8 \pm 35	-87 \pm 35	82.3 \pm 2.2	79.3 $^{+14.4}_{-13.0}$	2.5	7.5 $^{+3.0}_{-1.7}$	8.2 $^{+4.8}_{-4.6}$	✓

Table A4 – continued from previous page

ID (ACTPol-D56)	RA (deg)	dec (deg)	S/N	T _{CMB} (μK)	Stokes Q (μK)	Stokes U (μK)	S _{raw} (mJy)	S _{deb} (mJy)	S/N _p	pwk (%)	p _× (%)	pol ang (deg)	var?	V?	A?	S?
J010826-003722	17.1115	-0.6229	41.2	1168±28	-125±34	5±34	87.7±2.1	85.5 ^{+14.4} _{-13.9}	3.7	10.3 ^{+2.6} _{-2.8}	10.7 ^{+4.1} _{-4.1}	+77±5	..	✓	✓	..
J010838+013500	17.1615	+1.5835	449.7	13901±31	-197±32	-416±32	1043.4±2.3	..	14.3	3.3 ^{+0.3} _{-0.3}	3.2 ^{+0.3} _{-0.3}	-58±2	..	✓	..	✓
J011030-041532	17.6287	-4.2591	30.8	832±27	62.4±2.0	62.1 ^{+10.1} _{-10.0}	✓	✓	..
J011050-074143	17.7089	-7.6955	69.9	2200±31	-58±33	103±33	165.2±2.4	..	3.6	5.2 ^{+1.4} _{-1.4}	5.1 ^{+2.1} _{-2.1}	+60±8	..	✓	✓	..
J011239-032843	18.1630	-3.4787	65.2	1994±31	-42±32	-27±32	149.6±2.3	..	1.6	2.1 ^{+1.6} _{-0.8}	2.5 ^{+2.3} _{-2.3}	✓	✓	..
J011316-063052	18.3182	-6.5146	27.0	753±28	56.5±2.1	58.0 ^{+9.5} _{-9.5}	✓	✓	..
J011343+022217	18.4297	+2.3715	155.4	4430±29	-5±29	-1±29	332.5±2.1	0.0 ^{+0.3} _{-0.0}	0.0 ^{+1.0} _{-0.0}	✓
J011407+020809	18.5323	+2.1359	26.4	654±25	49.1±1.9	48.7 ^{+8.4} _{-8.0}	✓
J011429+000037	18.6229	+0.0104	16.4	462±28	34.6±2.1	33.8 ^{+6.0} _{-7.4}	✓
J011517-012700	18.8208	-1.4502	92.8	2979±32	-5±33	76±33	223.6±2.4	..	2.3	2.3 ^{+1.1} _{-0.6}	2.6 ^{+1.6} _{-1.6}	✓	✓	..
J011540+035645	18.9188	-3.9458	46.8	1392±30	25±35	-81±35	104.4±2.2	..	2.4	5.7 ^{+2.5} _{-1.3}	5.7 ^{+3.6} _{-3.6}	✓
J011727-042513	19.3662	+4.4205	30.5	803±26	60.3±2.0	60.5 ^{+9.8} _{-9.8}	✓	✓	..
J011818+025806	19.5771	+2.9685	112.0	3173±28	27±29	-20±29	238.1±2.1	..	1.2	0.7 ^{+1.0} _{-0.5}	0.7 ^{+1.3} _{-0.7}	✓
J011844-085059	19.6844	-8.8492	36.2	1615±45	9±53	-43±53	121.2±3.3	0.0 ^{+3.8} _{-0.0}	0.0 ^{+4.7} _{-0.0}
J012014-062652	20.0599	-6.4480	15.3	431±28	32.3±2.1	31.7 ^{+5.9} _{-6.2}	✓	✓	..
J012156+042226	20.4865	+4.3740	137.3	4270±31	66±32	-94±32	320.5±2.3	..	3.5	2.6 ^{+0.7} _{-0.7}	1.9 ^{+1.1} _{-1.1}	-27±9	..	✓
J012213-001758	20.5578	-0.2995	34.9	948±27	71.1±2.0	70.2 ^{+12.1} _{-11.8}	✓	✓	✓
J012217-005615	20.5729	-0.9375	23.6	633±27	47.5±2.0	48.1 ^{+8.2} _{-8.0}	✓	✓	..
J012335-034838	20.8990	-3.8106	44.6	1148±26	-58±31	-20±31	86.2±1.9	84.8 ^{+14.4} _{-13.8}	2.0	4.8 ^{+2.7} _{-1.4}	5.0 ^{+3.8} _{-3.8}	✓	✓	..
J012450-062501	21.2104	-6.4171	19.3	546±28	41.0±2.1	41.6 ^{+9.4} _{-9.3}	✓	✓	..
J012505+014632	21.2729	+1.7758	16.7	433±26	32.5±1.9	31.9 ^{+5.9} _{-6.1}	✓
J012528-000554	21.3698	-0.0984	194.1	5934±31	-77±31	-119±31	445.4±2.3	..	4.5	2.3 ^{+0.5} _{-0.5}	2.2 ^{+0.8} _{-0.8}	-61±7	..	✓	✓	✓
J012600-012041*	21.5026	-1.3449	52.3	1400±27	-4±32	32±32	105.1±2.0	..	1.1	0.7 ^{+2.6} _{-0.7}	2.3 ^{+0.0} _{-2.3}	✓	✓	✓
J012716-082129	21.8188	-8.3583	42.2	1180±28	36±33	-118±33	88.6±2.1	87.6 ^{+15.0} _{-14.6}	3.7	10.1 ^{+2.5} _{-2.7}	10.5 ^{+4.0} _{-4.0}	-36±8	..	✓	✓	..
J013241-080404	23.1719	-8.0678	25.0	664±27	49.8±2.0	49.6 ^{+8.5} _{-8.2}	✓	✓	..
J013412+000348	23.5526	-0.0635	29.1	779±27	58.5±2.0	59.5 ^{+9.7} _{-9.7}	✓
J013514-000701	23.8094	-0.1172	36.0	951±26	71.4±2.0	70.2 ^{+12.2} _{-12.2}	✓
J013852-054008	24.7167	-5.6691	37.9	979±26	73.5±1.9	72.1 ^{+12.3} _{-11.9}	✓	✓	..
J013957+013149	24.9885	+1.5304	104.9	2952±28	33±29	2±29	221.6±2.1	..	1.1	0.7 ^{+1.0} _{-0.5}	0.7 ^{+1.4} _{-0.7}	✓	..	✓
J014043+025445	25.1813	+2.9127	40.9	978±24	73.4±1.8	72.1 ^{+12.5} _{-11.9}	✓
J014133-020220	25.3906	-2.0390	49.4	1263±26	-22±30	36±30	94.8±1.9	95.7 ^{+16.1} _{-15.1}	1.4	2.7 ^{+2.4} _{-1.2}	1.3 ^{+3.4} _{-1.3}	✓	✓	..
J014239-054402	25.6625	-5.7341	37.8	955±25	71.7±1.9	70.6 ^{+13.1} _{-11.9}	✓	✓	..
J014316-011858	25.8193	-1.3163	23.2	605±26	45.4±2.0	47.1 ^{+7.6} _{-7.7}	✓	✓	..
J014609+004324	26.5406	+0.7235	34.8	849±24	63.7±1.8	63.2 ^{+11.0} _{-10.5}	✓
J014632+025627	26.6354	+2.9409	23.9	572±24	42.9±1.8	44.9 ^{+7.1} _{-10.4}	✓
J014721-044542	26.8391	-4.7617	33.6	841±25	63.1±1.9	63.0 ^{+10.8} _{-10.4}	✓	✓	..
J014738-082718	26.9099	-8.4551	35.9	1038±29	-41±34	-103±34	77.9±2.2	77.6 ^{+13.6} _{-10.7}	3.2	10.3 ^{+3.2} _{-3.1}	10.6 ^{+4.8} _{-4.8}	-56±10	..	✓	✓	..
J014816+001946	27.0677	+0.3297	33.2	832±25	62.4±1.9	62.1 ^{+10.0} _{-10.0}	✓	..	✓
J014934-073318	27.3922	-7.5552	36.7	946±26	71.0±1.9	70.2 ^{+12.1} _{-11.8}	✓
J015239+014719	28.1651	+1.7888	26.3	628±24	47.1±1.8	47.3 ^{+7.8} _{-7.8}	✓
J015243+002041	28.1797	+0.3448	53.3	1341±25	-16±30	-48±30	100.7±1.9	..	1.7	3.3 ^{+2.2} _{-1.2}	3.2 ^{+3.2} _{-3.2}	✓	..	✓
J015422-023453	28.5948	-2.5816	29.0	706±24	53.0±1.8	53.3 ^{+9.5} _{-8.9}	✓	✓	..
J015500+004952	28.7510	+0.8313	18.1	452±25	33.9±1.9	33.6 ^{+8.9} _{-7.2}	✓
J015553-062135	28.9724	-6.3599	17.2	471±27	35.4±2.1	34.3 ^{+6.3} _{-7.6}	✓
J015710+001126	29.2938	+0.1906	24.8	627±25	47.1±1.9	47.3 ^{+7.8} _{-7.8}	✓
J020004+012513	30.0167	+1.4205	20.3	486±24	36.5±1.8	35.6 ^{+6.1} _{-7.8}	✓
J020040+032248	30.1703	+3.3801	78.0	2304±30	28±30	-79±30	173.0±2.2	..	2.7	3.4 ^{+1.3} _{-1.3}	2.2 ^{+1.9} _{-1.9}	✓
J020137-002346	30.4073	-0.3964	20.7	530±26	39.8±1.9	40.1 ^{+7.2} _{-9.3}	✓
J020151+034307	30.4651	+3.7188	21.8	589±27	44.2±2.0	45.8 ^{+7.3} _{-10.4}	✓
J020207-055901	30.5292	-5.9838	67.5	1984±29	18±30	-38±30	148.9±2.2	..	1.4	1.7 ^{+1.5} _{-0.8}	2.0 ^{+2.2} _{-2.0}	✓	✓	..
J020214-001748	30.5599	-0.2969	29.8	763±26	57.3±1.9	58.6 ^{+9.6} _{-9.6}	✓	✓	✓	..
J020224-014506	30.6037	-1.7518	24.6	622±25	46.7±1.9	47.3 ^{+7.8} _{-7.8}	✓
J020234+000301	30.6427	+0.0505	33.0	828±25	62.2±1.9	62.1 ^{+10.1} _{-10.0}	✓
J020354+023555	30.9781	+2.5988	40.4	935±23	70.2±1.7	69.3 ^{+12.0} _{-11.5}	✓
J020529+040321	31.3729	+4.0560	18.4	514±28	38.6±2.1	38.1 ^{+7.2} _{-8.4}	✓
J020826-003228	32.1089	-0.5412	17.1	439±26	32.9±1.9	32.4 ^{+5.9} _{-6.2}	✓
J020826-004741	32.1099	-0.7948	60.8	1820±30	-75±31	55±31	136.6±2.2	..	3.0	4.8 ^{+1.6} _{-1.6}	5.2 ^{+2.4} _{-2.4}	+71±10	..	✓	✓	✓
J020931-043827	32.3792	-4.6410	26.4	649±25	48.7±1.8	48.4 ^{+8.3} _{-8.0}	✓	✓	..
J020931-073648	32.3807	-7.6135	24.0	618±26	46.4±1.9	47.3 ^{+7.7} _{-7.7}	✓	✓	..
J021053-063336	32.7229	-6.5602	15.4	411±27	30.8±2.0	30.1 ^{+6.0} _{-5.9}	✓
J021316-071932	33.3203	-7.3257	32.5	824±25	61.8±1.9	61.9 ^{+9.9} _{-9.8}	✓	✓	..
J021541-022256	33.9245	-2.3825	47.5	1148±24	69±29	-57±29	86.1±1.8	84.9 ^{+14.3} _{-13.9}	3.1	7.4 ^{+2.4} _{-2.4}	6.2 ^{+3.6} _{-3.6}	-20±10	..	✓	✓	..

Table A4 – continued from previous page

ID (ACTPol-D56)	RA (deg)	dec (deg)	S/N	T _{CMB} (μK)	Stokes Q (μK)	Stokes U (μK)	S _{raw} (mJy)	S _{deb} (mJy)	S/N _p	p _{WK} (%)	p _× (%)	pol ang (deg)	var?	V?	A?	S?
J021553+001826	33.9740	+0.3073	17.8	437±25	32.8±1.8	32.4 ^{+5.9} _{-6.2}	✓
J021555+052427	33.9800	+5.4075	27.0	933±35	70.0±2.6	68.9 ^{+12.1} _{-11.4}
J021702-082051	34.2609	-8.3477	118.7	3746±32	297±32	-66±32	281.2±2.4	..	9.3	8.1 ^{+0.9} _{-1.0}	8.2 ^{+1.2} _{-1.2}	-6±3	..	✓	✓	..
J021749+014449	34.4542	+1.7472	338.7	8943±26	-148±28	-101±28	671.2±2.0	..	6.4	2.0 ^{+0.3} _{-0.3}	2.0 ^{+0.4} _{-0.4}	-73±5	..	✓	..	✓
J021835+004039	34.6484	+0.6776	34.2	817±24	61.3±1.8	61.4 ^{+9.8} _{-9.8}	✓
J021907+012100	34.7792	+1.3501	123.8	3287±27	..	-167±27	246.7±2.0	..	6.1	5.0 ^{+0.8} _{-0.9}	4.7 ^{+1.2} _{-1.2}	-45±5	..	✓
J021920-025842	34.8370	-2.9784	39.9	957±24	71.9±1.8	70.9 ^{+12.1} _{-12.0}
J022146-013306	35.4443	-1.5518	28.7	708±25	53.1±1.9	53.9 ^{+9.5} _{-9.4}	✓	✓
J022152+023614	35.4698	+2.6040	23.0	526±23	39.5±1.7	39.3 ^{+7.4} _{-7.4}	✓
J022313-020505	35.8042	-2.0848	29.7	731±25	54.9±1.8	56.2 ^{+9.6} _{-9.5}	✓	✓	..
J022430-021932	36.1260	-2.3256	17.7	433±24	32.5±1.8	31.9 ^{+5.9} _{-6.1}	✓	✓
J022640-055239	36.6667	-5.8775	34.7	881±25	66.1±1.9	64.6 ^{+11.3} _{-10.7}	✓	..	✓
J022853-033736	37.2219	-3.6269	66.5	1872±28	45±29	-63±29	140.5±2.1	..	2.7	3.9 ^{+1.6} _{-1.6}	2.7 ^{+2.2} _{-2.2}	✓	✓	✓
J023322-045504	38.3422	-4.9180	29.3	742±25	55.7±1.9	56.9 ^{+9.6} _{-9.5}	✓	✓	✓	..
J023330-020320	38.3766	-2.0557	21.4	517±24	38.8±1.8	38.1 ^{+7.2} _{-8.4}	✓	✓
J023507-040206	38.7807	-4.0351	39.3	961±24	72.1±1.8	71.0 ^{+12.2} _{-11.3}	✓	✓	..
J023919+025109	39.8297	+2.8527	19.6	496±25	37.2±1.9	36.3 ^{+6.9} _{-7.9}	✓
J023945-023440	39.9391	-2.5780	116.6	3270±28	-24±29	-32±29	245.4±2.1	..	1.4	1.0 ^{+0.9} _{-0.5}	0.7 ^{+1.3} _{-0.7}	✓	✓	..
J023951+041623	39.9630	+4.2732	156.5	7035±45	96±47	252±47	528.0±3.4	..	5.8	3.8 ^{+0.7} _{-0.7}	3.7 ^{+0.9} _{-0.9}	+34±5	..	✓
J024056-050440	40.2333	-5.0780	53.6	1847±34	-7±41	-28±41	138.6±2.6	0.0 ^{+2.3} _{-0.0}	1.5 ^{+0.0} _{-1.5}	✓	✓	..
J024104-081514	40.2698	-8.2540	274.7	11652±42	69±44	-39±44	874.6±3.2	..	1.8	0.6 ^{+0.4} _{-0.2}	0.5 ^{+0.3} _{-0.5}	✓	✓	..
J024145+002645*	40.4385	+0.4458	24.6	619±25	46.5±1.9	47.3 ^{+7.7} _{-7.7}	✓
J232839-063433	352.1635	-6.5759	29.0	991±34	74.4±2.6	73.4 ^{+12.3} _{-11.8}	✓	✓	..
J232925+050310	352.3557	+5.0529	16.1	906±56	68.0±4.2	67.1 ^{+10.9} _{-10.9}	✓
J233316-013108	353.3193	-1.5189	39.3	1128±29	-92±34	16±34	84.7±2.2	82.4 ^{+14.8} _{-13.8}	2.7	7.8 ^{+3.0} _{-3.1}	7.9 ^{+4.4} _{-4.4}	..	✓	✓	✓	..
J233520-013110	353.8349	-1.5195	186.9	6206±33	-35±34	92±34	465.8±2.5	..	2.9	1.5 ^{+0.6} _{-0.6}	1.4 ^{+0.8} _{-0.8}	✓	✓	✓
J233552-003458	353.9672	-0.5828	16.8	486±29	36.5±2.2	35.6 ^{+6.7} _{-7.8}	✓	✓	..
J233757-023057	354.4891	-2.5159	122.4	3829±31	-132±32	12±32	287.4±2.3	..	4.1	3.4 ^{+0.8} _{-0.8}	3.5 ^{+1.2} _{-1.2}	+80±5	✓	..	✓	✓
J233807+032652	354.5323	+3.4479	34.4	1091±32	32±38	..	81.9±2.4	78.8 ^{+14.0} _{-12.9}	..	0.0 ^{+0.0} _{-0.0}	2.6 ^{+0.0} _{-2.6}	✓
J233853-072103	354.7245	-7.3509	17.8	538±30	40.4±2.3	41.1 ^{+7.2} _{-9.4}	✓
J233929+024407	354.8740	+2.7354	55.4	1672±30	-8±31	-36±31	125.5±2.3	..	1.2	1.5 ^{+1.9} _{-0.8}	2.0 ^{+2.7} _{-1.0}	✓
J234106+001830	355.2787	+0.3083	21.0	588±28	44.2±2.1	45.8 ^{+7.3} _{-10.4}	✓	..	✓
J234110-034156	355.2927	-3.6989	16.7	459±27	34.4±2.1	33.8 ^{+5.9} _{-7.4}	✓	✓	..
J234357-052150	355.9875	-5.3641	31.5	898±29	67.4±2.1	66.2 ^{+11.8} _{-11.0}	✓	✓	..
J234656-020344	356.7333	-2.0624	28.0	770±28	57.8±2.1	59.2 ^{+9.7} _{-9.7}	✓	✓
J234811-042557	357.0490	-4.4326	52.5	1403±27	-31±32	59±32	105.3±2.0	..	2.1	4.3 ^{+2.3} _{-1.2}	4.3 ^{+3.2} _{-3.2}	✓	✓	..
J234910-043805	357.2917	-4.6347	27.2	733±27	55.0±2.0	56.2 ^{+9.6} _{-9.5}	✓	✓	..
J235050-002846	357.7120	-0.4797	14.9	420±28	31.5±2.1	30.5 ^{+6.1} _{-6.1}	✓
J235054-042701	357.7260	-4.4503	32.2	870±27	65.3±2.0	64.1 ^{+11.3} _{-10.7}	✓
J235156-010917	357.9844	-1.1548	23.4	671±29	50.4±2.2	50.2 ^{+8.5} _{-8.3}	✓	✓	..
J235409-001946	358.5375	-0.3297	29.0	834±29	62.6±2.2	62.0 ^{+10.2} _{-10.0}	✓	✓	..
J235451-040503	358.7162	-4.0842	24.0	647±27	48.5±2.0	48.2 ^{+8.2} _{-7.9}	✓	✓	..
J235524-072946	358.8526	-7.4964	22.6	616±27	46.2±2.0	47.3 ^{+7.7} _{-7.7}	✓	✓	..
J235706+044859	359.2787	+4.8166	22.5	621±28	46.6±2.1	47.3 ^{+7.8} _{-7.8}	✓
J235725-015214	359.3542	-1.8706	32.1	892±28	67.0±2.1	65.9 ^{+11.7} _{-10.9}	✓	✓	✓	..
J235809-080005	359.5406	-8.0015	16.0	436±27	32.7±2.0	32.3 ^{+5.8} _{-6.2}	✓
J235828+043024	359.6193	+4.5067	30.8	939±30	70.5±2.3	69.5 ^{+12.0} _{-11.6}	✓	✓
J235931-063940	359.8828	-6.6614	38.8	1108±29	-26±34	-26±34	83.2±2.1	81.7 ^{+14.7} _{-13.6}	1.1	1.7 ^{+3.2} _{-1.6}	2.1 ^{+4.4} _{-2.1}	✓	✓	..
J235936-003115	359.9037	-0.5208	25.2	736±29	55.3±2.2	56.4 ^{+9.6} _{-9.6}	✓	✓	✓	..